

single-phase displacements. Decane (C_{10}) with undecane (C_{11}) as a tracer was used for the oil phase displacement. Results of refractive index calibrations for C_{10} - C_{11} mixtures are shown in Fig. 4.13. Clearly, the response is linear over the range of compositions to be used, 0 to 5 vol % C_{11} in C_{10} . To be suitable for use in the core flood experiments, the displaced and displacing fluids should have matched densities and viscosities. Fig. 4.14 shows results of viscosity measurements for C_{10} - C_{11} mixtures. The viscosities of pure C_{10} and C_{10} containing 5 vol % C_{11} differ by only 1%. Densities of the pure components at 20°C are 0.7301 (C_{10}) and 0.7402 g/cm³ (C_{11}). If there were no volume change on mixing, a good assumption for mixtures of normal alkanes, the density difference between pure C_{10} and C_{10} + 5 vol % C_{11} would be less than 0.1%. Thus, the C_{10} - C_{11} mixtures meet the requirement for fluids of matched density and viscosity.

As in the single-phase displacements, on-line data acquisition with a microcomputer allows displacement data to be collected rapidly for runs at different displacement velocities.

4.3 Interpretation of Displacement Experiments

Typical results of miscible displacements in carbonate and sandstone core samples are shown in Fig. 4.15. In those early displacements, the core was filled with ethylbenzene and a slug of approximately one-half pore volume of ethylbutyrate was injected. Those fluids also have matched density and viscosity. Clearly, the displacement behavior of the sandstone differed substantially from that of the carbonate. The slug arrived at about one pore volume injected (PVI) in the sandstone but appeared at about 0.6 PVI in the carbonate. In the sandstone displacement, the slug was completely recovered at 2 PVI while small amounts of the slug material were still being produced at 4 PVI in the carbonate.

As was described in §4.1, the simplest model which can produce the effluent composition behavior shown in Fig. 4.16 is that offered by Coats and Smith (1964) in which the pore space is represented as flowing and stagnant fractions between which mass transfer can occur. The model has the form

$$f \frac{\partial c}{\partial \tau} + (1 - f) \frac{\partial c^*}{\partial \tau} + \frac{\partial c}{\partial \xi} - \frac{1}{Pe} \frac{\partial^2 c}{\partial \xi^2} = 0 \quad 0 \leq \xi \leq 1$$

$$\tau > 0 \quad (4.8)$$

$$(1 - f) \frac{\partial c^*}{\partial \tau} = a (c - c^*)$$

where f is the flowing fraction, c the volume fraction of injected slug in the flowing stream, τ the dimensionless time scale in pore volumes, c^* the volume fraction of slug material in the stagnant volume, ξ the dimensionless length scale, Pe the Peclet number, and a the dimensionless mass transfer group. Thus, the solution to (4.8) is determined by three parameters, the flowing fraction, the Peclet number and the mass transfer group where

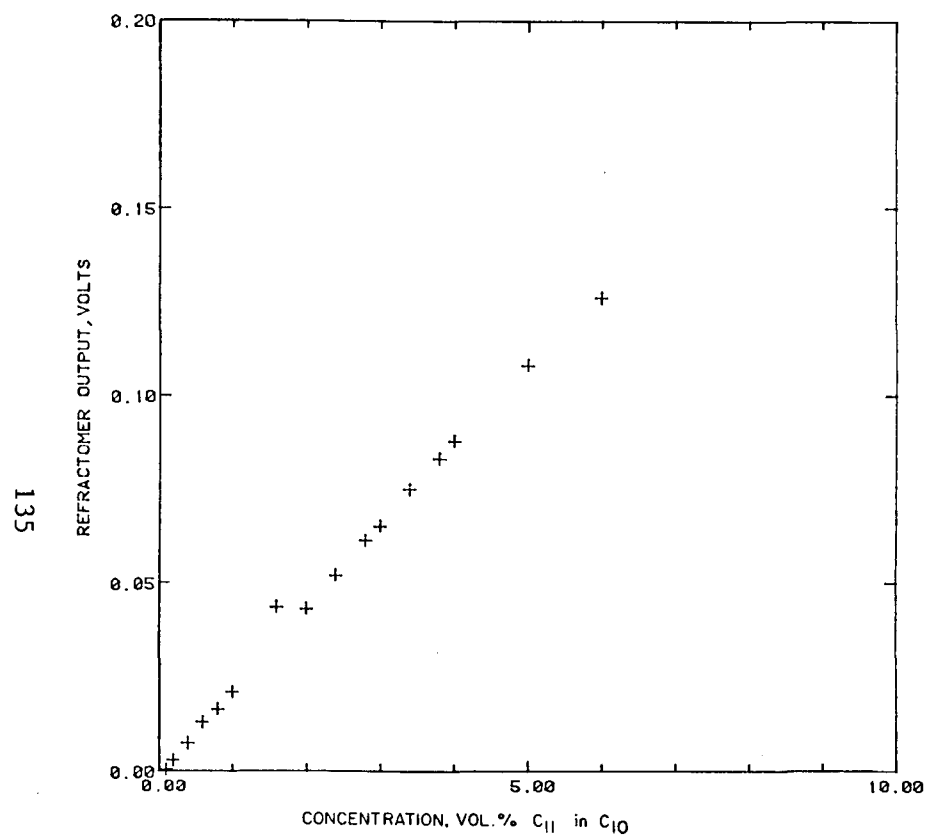


Fig. 4.13 Differential refractometer output for C₁₀-C₁₁ mixtures. The reference fluid was C₁₀.

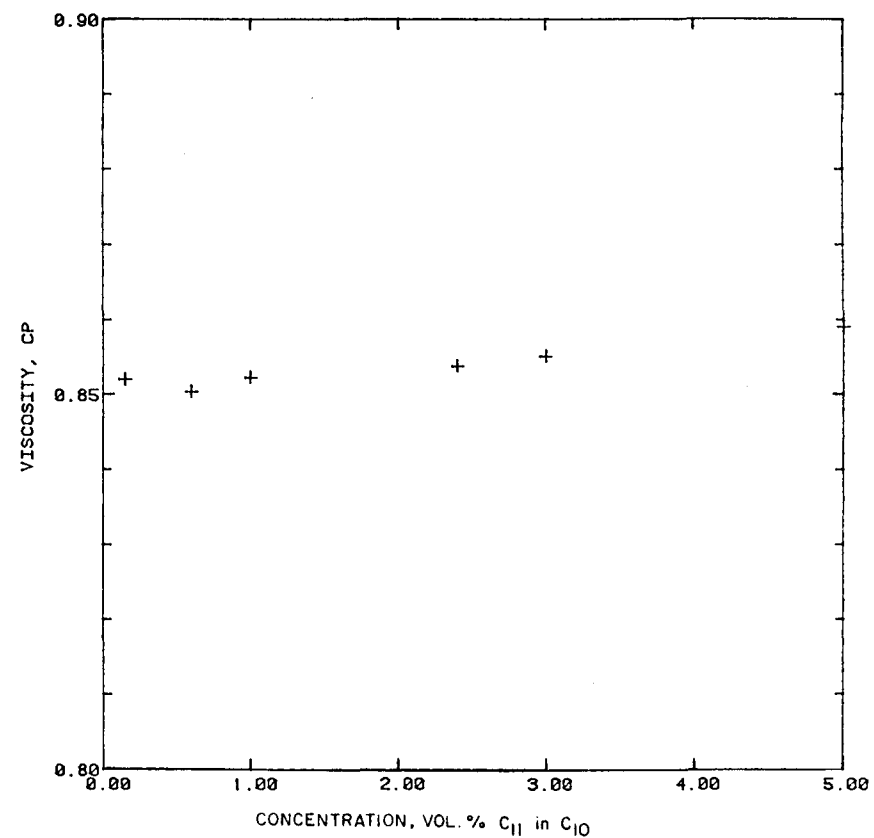


Fig. 4.14 Viscosity of C₁₀-C₁₁ mixtures at 25°C.

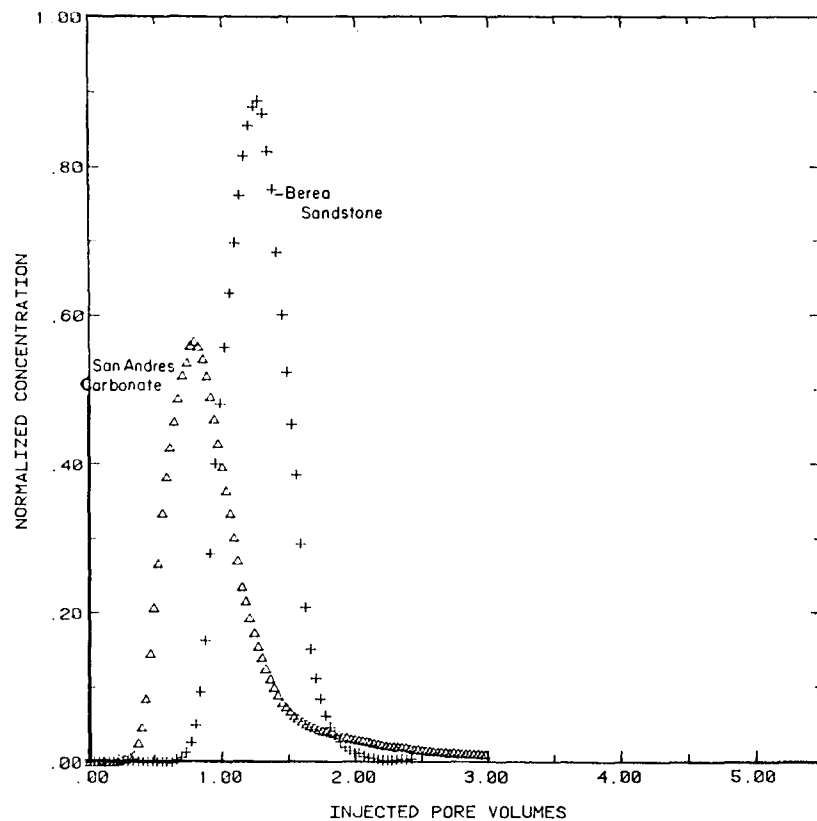


Fig. 4.15 Comparison of miscible displacements in a carbonate (Seminole San Andres) and a sandstone (Berea).

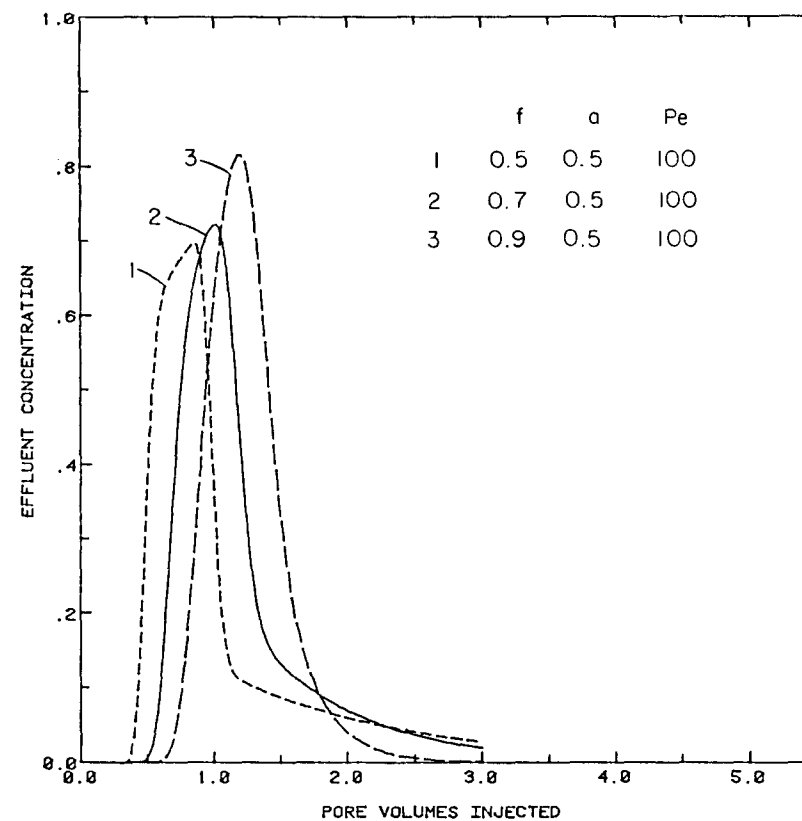


Fig. 4.16 Effect of variations in flowing fraction, f , on effluent compositions calculated with the Coats-Smith model.

$$Pe = \frac{uL}{D} \quad (4.9)$$

$$a = \frac{KL}{u}$$

where u is the average interstitial flow velocity or $q/\phi A$, L the length of the core, D the dispersion coefficient, and K the mass transfer coefficient. Eq. (4.8) was solved using an explicit finite difference method with the following initial and boundary conditions:

$$\begin{aligned} c &= c^* = 0, \quad \tau = 0, \quad 0 \leq \xi \leq 1 \\ c - \frac{1}{Pe} \frac{\partial c}{\partial \xi} &= 1, \quad 0 < \tau < \beta, \quad \xi = 0 \\ c - \frac{1}{Pe} \frac{\partial c}{\partial \xi} &= 0, \quad \beta < \tau, \quad \xi = 0 \\ \frac{\partial c}{\partial \xi} &= 0, \quad \tau > 0, \quad \xi = 1 \end{aligned} \quad (4.10)$$

Eq. (4.8) was solved analytically by Coats and Smith for slightly different boundary conditions using a Laplace transform. The method used here avoids the evaluation of the semi-infinite integrals required for inversion of the Laplace transform but requires the use of small time steps. The finite difference form of (4.8) is

$$\begin{aligned} c_i^{k+1} &= c_i^k - \frac{a\Delta\tau}{f} \left(c_i^k - c_i^{*k} \right) - \frac{\Delta\tau}{f\Delta\xi} \left(c_i^k - c_{i-1}^k \right) \\ &\quad + \frac{\Delta\tau}{f\Delta\xi^2 Pe} \left[c_{i+1}^k - 2c_i^k + c_{i-1}^k \right] \\ c_i^{*k+1} &= c_i^{*k} + \frac{a\Delta\tau}{f} \left(c_i^k - c_i^{*k} \right) \end{aligned} \quad (4.11)$$

Solutions obtained with eq. (4.9) are shown in Figs. 4.16-4.18. Fig. 4.16 illustrates the effect of changing the flowing fraction with the mass transfer group and Peclet number held constant. Clearly, decreasing the flowing fraction causes the slug to arrive sooner at the outlet. Peak height also declines as mass transfer into the increasing stagnant volume increases, and there is a corresponding lengthening of the tail of the slug as the material in the stagnant volume transfers back into the flowing stream. The effect of changing the mass transfer group is shown in Fig. 4.17. An increase in that group causes a reduction in the peak height, with a corresponding increase in the concentration of slug material in the tail. Fig. 4.18 shows the effect of changes in the Peclet number. An increase in the Peclet number broadens the peak and causes a decrease in the peak height.

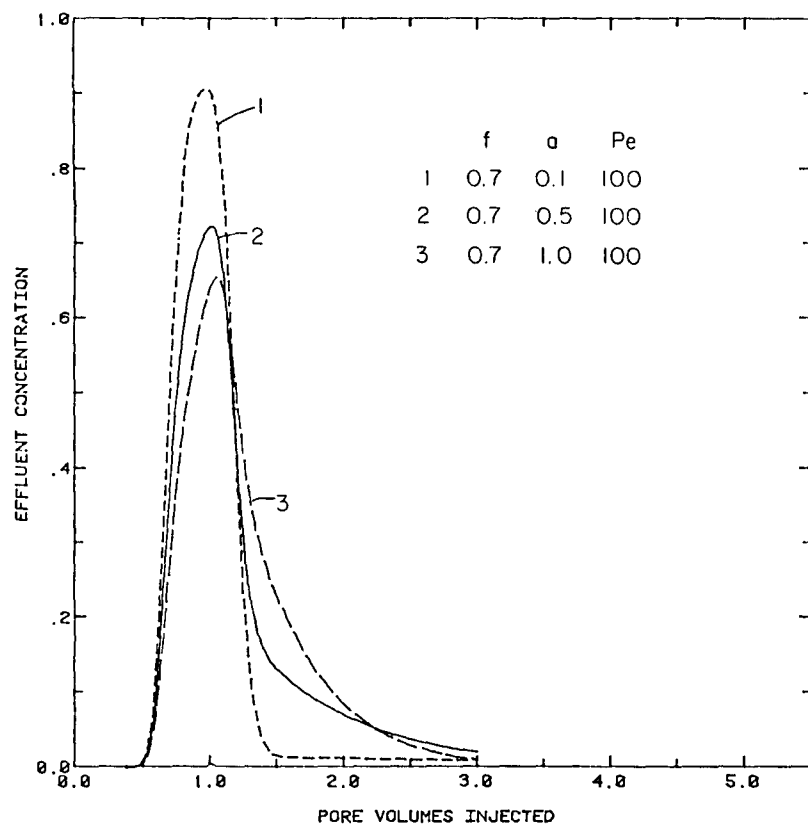


Fig. 4.17 Effect of variations in Damköhler number, a , on effluent compositions calculated with the Coats-Smith model.

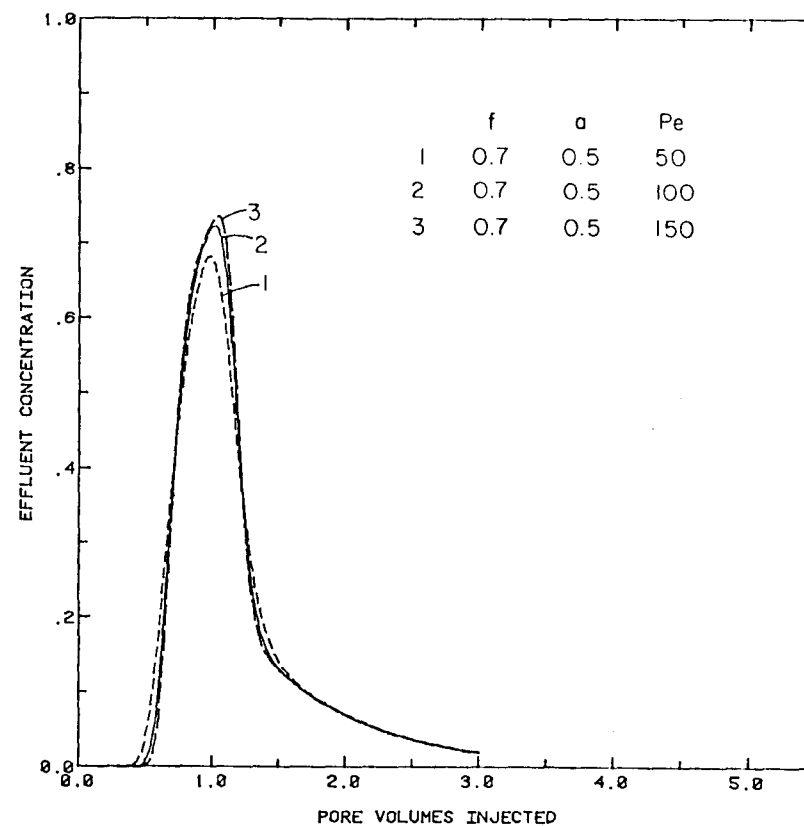


Fig. 4.18 Effect of variations in Peclet number, Pe , on effluent compositions calculated with the Coats-Smith model.

Examination of Figs. 4.16-4.18 along with results of computations over a range of parameter values leads to the following observations:

- The arrival time of the leading edge of the pulse is most sensitive to the value of f .
- The concentration of slug material is determined by the mass transfer group, if the flowing fraction is fixed.

These observations are the basis of the scheme (described below) used to obtain initial estimates of the values of the three parameters for displacement experiments.

Numerical Dispersion

The solutions presented in Figs. 4.16-4.18 were all affected by numerical dispersion, which arises from truncation error in the numerical representation of the first derivative terms in eq. (4.8). In fact, the actual Peclet number for a numerical solution using eq. (4.11) is the sum of the entered value and a numerical contribution,

$$Pe^t = Pe^e + Pe^n \quad (4.12)$$

where Pe^t is the total Peclet number, Pe^e is the value used in eq. (4.11), and Pe^n is the numerical contribution. The numerical contribution can be evaluated by a procedure similar to that of Lantz (1971) for miscible displacement in a uniform porous medium. The backward space and forward time finite difference representations of the derivatives in eq. (4.8) are

$$\begin{aligned} \frac{c_i^{k+1} - c_i^k}{\Delta\tau} &= \frac{\partial c}{\partial \tau} + \frac{1}{2} \Delta\tau \frac{\partial^2 c}{\partial \tau^2} + \dots \\ \frac{c_i^k - c_{i-1}^k}{\Delta\xi} &= \frac{\partial c}{\partial \xi} - \frac{1}{2} \Delta\xi \frac{\partial^2 c}{\partial \xi^2} + \dots \end{aligned} \quad (4.13)$$

$$\frac{c_{i+1}^k - 2c_i^k + c_{i-1}^k}{\Delta\xi^2} = \frac{\partial^2 c}{\partial \xi^2} + \frac{\Delta\xi^2}{12} \frac{\partial^4 c}{\partial \xi^4} + \dots$$

If the expressions given as eq. (4.13) are substituted into eq. (4.11), then the equation actually being solved is

$$\begin{aligned} f \frac{\partial c}{\partial \tau} + (1-f) \frac{\partial c^*}{\partial \tau} + \frac{\partial c}{\partial \xi} - \frac{1}{Pe} \frac{\partial^2 c}{\partial \xi^2} \\ \frac{1}{2} (1-f) \Delta\tau \frac{\partial^2 c^*}{\partial \tau^2} + \frac{f}{2} \Delta\tau \frac{\partial^2 c}{\partial \tau^2} - \frac{1}{2} \Delta\xi \frac{\partial^2 c}{\partial \xi^2} = 0 \end{aligned} \quad (4.14)$$

if derivatives higher than second order are neglected. Thus, the finite difference version includes additional second order terms proportional to the time step and grid block sizes. In fact, $\partial^2 c / \partial \tau^2$ and $\partial^2 c / \partial \xi^2$ are of comparable size. Differentiation of the first equation of eq. (4.8) with respect to τ yields

$$f \frac{\partial^2 c}{\partial \tau^2} + (1 - f) \frac{\partial^2 c^*}{\partial \tau^2} + \frac{\partial^2 c}{\partial \tau \partial \xi} - \frac{1}{Pe} \frac{\partial^3 c}{\partial \tau \partial \xi^2} = 0 \quad (4.15)$$

Similarly, differentiation with respect to ξ gives

$$f \frac{\partial^2 c}{\partial \xi \partial \tau} + (1 - f) \frac{\partial^2 c^*}{\partial \xi \partial \tau} + \frac{\partial^2 c}{\partial \xi^2} - \frac{1}{Pe} \frac{\partial^3 c}{\partial \xi^3} = 0 \quad (4.16)$$

Subtraction of (4.16) from (4.15) gives

$$\begin{aligned} f \frac{\partial^2 c}{\partial \tau^2} + (1 - f) \frac{\partial^2 c^*}{\partial \tau^2} + (1 - f) \left[\frac{\partial^2 c}{\partial \tau \partial \xi} - \frac{\partial^2 c^*}{\partial \tau \partial \xi} \right] \\ - \frac{\partial^2 c}{\partial \xi^2} + \frac{1}{Pe} \left[\frac{\partial^3 c}{\partial \xi^3} - \frac{\partial^3 c}{\partial \tau \partial \xi^2} \right] = 0 \end{aligned} \quad (4.17)$$

Now consider the second and third terms in (4.17). From the original equation for mass transfer into the stagnant volume,

$$(1 - f) \frac{\partial c^*}{\partial \tau} \leq a (c - c^*) \quad (4.18)$$

so differentiation twice with respect to τ gives

$$\frac{(1 - f)}{a} \frac{\partial^3 c^*}{\partial \tau^3} = a \left(\frac{\partial^2 c}{\partial \tau^2} - \frac{\partial^2 c^*}{\partial \tau^2} \right) \quad (4.19)$$

and hence

$$\frac{\partial^2 c^*}{\partial \tau^2} = \frac{\partial^2 c}{\partial \tau^2} - \frac{(1 - f)}{a} \frac{\partial^3 c^*}{\partial \tau^3} \quad (4.20)$$

Differentiation of (4.18) with respect to τ and then ξ gives

$$(1 - f) \frac{\partial^3 c^*}{\partial \tau^2 \partial \xi} = a \left(\frac{\partial^2 c}{\partial \tau \partial \xi} - \frac{\partial^2 c^*}{\partial \tau \partial \xi} \right) \quad (4.21)$$

from which

$$(1 - f) \left(\frac{\partial^2 c}{\partial \tau \partial \xi} - \frac{\partial^2 c^*}{\partial \tau \partial \xi} \right) = \frac{(1 - f)^2}{a} \frac{\partial^3 c^*}{\partial \tau^2 \partial \xi} \quad (4.22)$$

Substitution of (4.20) and (4.22) into (4.17) gives

$$f \frac{\partial^2 c}{\partial \tau^2} + (1-f) \left[\frac{\partial^2 c}{\partial \tau^2} - \frac{(1-f)}{a} \frac{\partial^3 c^*}{\partial \tau^3} \right] + \frac{(1-f)^2}{a} \frac{\partial^3 c^*}{\partial \tau^2 \partial \xi} \quad (4.23)$$

$$- \frac{\partial^2 c}{\partial \xi^2} + \frac{1}{Pe} \left[\frac{\partial^3 c}{\partial \xi^3} - \frac{\partial^3 c}{\partial \tau \partial \xi^2} \right] = 0$$

If derivatives higher than second order are neglected, then

$$\frac{\partial^2 c}{\partial \tau^2} \approx \frac{\partial^2 c}{\partial \xi^2} \quad (4.24)$$

From (4.14) then,

$$f \frac{\partial c}{\partial \tau} + (1-f) \frac{\partial c^*}{\partial \tau} + \frac{\partial c}{\partial \xi} - \left[\frac{1}{Pe} + \frac{1}{2} (\Delta \xi - \Delta \tau) \right] \frac{\partial^2 c}{\partial \xi^2} = 0 \quad (4.25)$$

Thus, the numerical contribution to the total Peclet number is

$$Pe^n = [\frac{1}{2}(\Delta \xi - \Delta \tau)]^{-1} \quad (4.26)$$

Hence, the numerical dispersion for this finite difference model is exactly the same as that for miscible displacement in a uniform porous medium. Eq. (4.26) is a useful result. Because the numerical contribution to the total Peclet number can be estimated quantitatively, numerical dispersion need not be reduced to a very low level. Instead, the finite difference solution can be obtained inexpensively with relatively large grid blocks and time steps and the effect of numerical dispersion accounted for with eq. (4.26).

The accuracy of the estimate given as eq. (4.26) is indicated in Figs. 4.19 and 4.20, which show results of three solutions with constant values of f (0.7), a (0.5) and total Peclet number (100). Grid block and time step sizes were different in the three cases, however. Table 4.1 gives values of $\Delta \tau$ and $\Delta \xi$ along with values of Pe^e and Pe^n . Fig. 4.19 is a plot of the three solutions, which are indistinguishable on the scale of the plot. Fig. 4.20 shows the difference between the calculated solution for $\Delta \xi = .005$ and those for the runs with larger grid blocks. The absolute differences and the percent errors are small, except where the solutions are nearly zero. The small differences between solutions confirm that numerical dispersion can be used to represent a portion of the total dispersion.

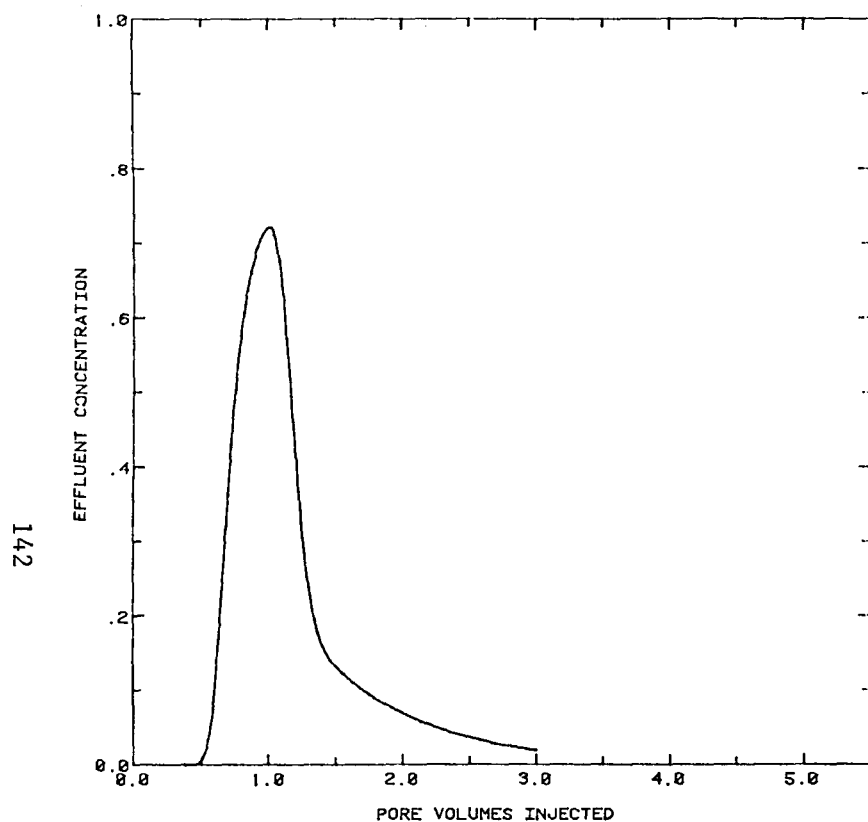


Fig. 4.19 Comparison of three solutions of the Coats-Smith model with different levels of numerical dispersion but constant total Peclet number.

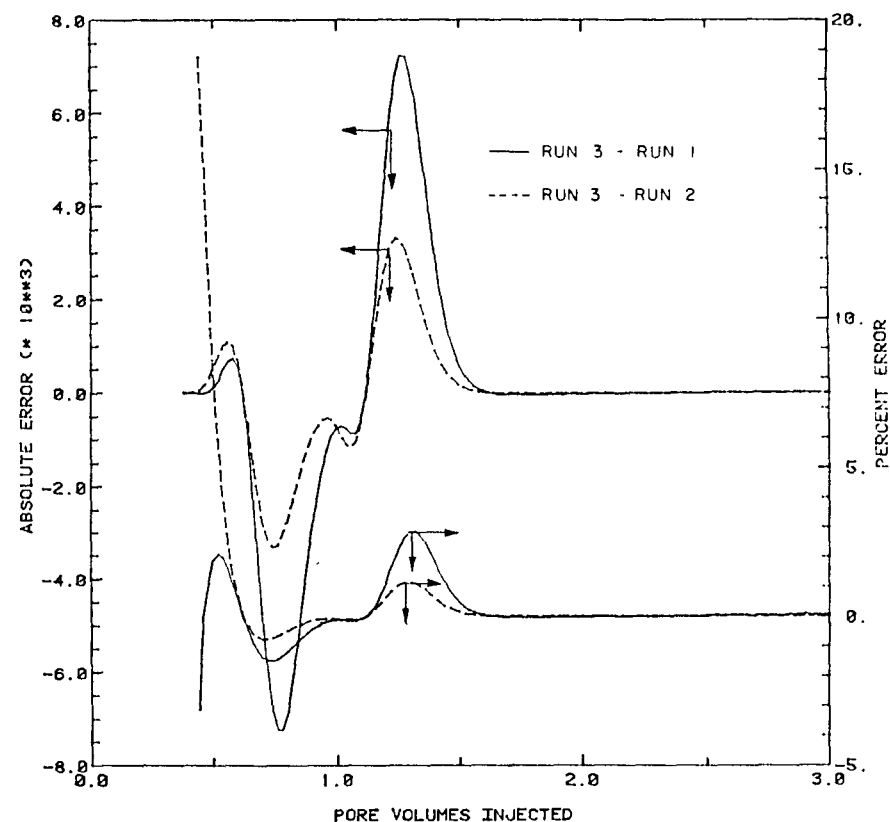


Fig. 4.20 Differences between Coats-Smith solutions with different levels of numerical dispersion but constant total Peclet number.

Table 4.1 Grid Block and Time Step Sizes for Tests
of the Effects of Numerical Dispersion

<u>Run</u>	<u>$\Delta\xi$</u>	<u>$\Delta\tau$</u>	<u>Pe^n</u>	<u>Pe^e</u>	<u>Pe^{tot}</u>
1	.02	.004	125	500	100
2	.01	.002	250	167	100
3	.005	.0008	476	127	100

Parameter Estimation

A modification of Powell's algorithm (Powell 1964) was used to determine values of f , a and Pe for several displacements. The objective function was defined to be the sum of the absolute values of the differences between the calculated and experimental effluent compositions. The total error was divided into three parts. The leading edge error was defined to be the sum of the absolute errors for all effluent concentrations ahead of the peak concentration (Fig. 4.15). Trailing edge error was defined as the sum of errors between the peak value and the time at which the slope of the effluent concentration curve had declined to -0.2 . Tail error was defined as the sum of errors after the end of the trailing edge. The algorithm to determine parameters had two parts. In the first, initial estimates of the parameters were obtained. In the second, a detailed minimization was performed using Powell's method. The algorithm used was:

- (1) Minimize leading edge error by adjusting f .
- (2) Minimize the sum of leading and trailing edge error by adjusting Pe .
- (3) Minimize the total error by adjusting a .

The values of f , Pe and a so obtained were used as the initial guess for Powell's method. Use of a separate method for generating reasonable initial guesses reduced computation time by about 25% below the application of Powell's algorithm from the beginning.

Two-Phase Displacements

As Salter and Mohanty (1982) pointed out, when two immiscible phases exist in a porous media, there is a possibility that one phase may isolate and disconnect (trap) portions of a second phase from the second phase flow paths. When trapping occurs, the flow behavior of the non-isolated portion of the phase may be adequately described by a three parameter, Coats-Smith model, eq. (4.8). The parameters must, however, be based on the untrapped phase pore volume and average velocity in the non-isolated phase pore space. The trapped volume (or its complement, the untrapped volume) may be determined by a mass balance on the fluid present in the core initially in a step-input displacement. Then the procedure described above for a single-phase displacement can be used to determine the best fit parameters, Pe , a or f , based on the untrapped pore volume. The dispersion and mass transfer coefficients may be calculated using the average interstitial velocity based on the untrapped pore volume

$$u_i = \frac{q_i}{\phi A S_i (1 - f_t^i)} \quad (4.27)$$

where u_i is the average interstitial velocity of phase i , cm/sec; q_i the volume flow rate of phase i , cm³/sec; ϕ porosity; A the total cross-sectional

area, cm^2 ; S_i the total steady-state saturation of phase i ; and f_t the trapped fraction of the phase i pore volume.

4.4 Results of Displacement Experiments

Properties of sandstone and carbonate cores used in this study are reported in Tables 4.2 and 4.3. Results of single-phase displacements at several velocities in each core are summarized in Table 4.4 for the sandstone cores and in Table 4.5 for the carbonates. Results of two-phase displacements are reported in Table 4.6.

Single-Phase Displacements: Sandstone Cores

Typical results of displacements in the three sandstones, Berea, Frannie and Rock Creek, are shown in Figs. 4.21-4.23. Values of Coats-Smith parameters (f , a , Pe , D and K_m), the flow velocity u , and the pulse size in pore volumes β are shown on the plots as well as in Table 4.4. Also shown are the total error, defined as the sum of the absolute values of the difference between the calculated and measured composition at each data point, the number of data points used and the overall mass balance, V_o/V_{in} , defined as the volume of pulse fluid produced divided by the volume of pulse fluid injected. Those data give some indication of the quality of the data and the history match. Effluent concentration plots are given in Appendix B for all of the displacements listed in Tables 4.4 and 4.5. Differences between the displacements were minimal. In all the displacements the 50% concentration appeared at about one pore volume injected, and there was little tailing. Differences in peak height were due primarily to differences in dimensionless pulse volume which result when the same injection loop is used with cores having different pore volumes. Dispersion coefficients determined using least squares fits of a straight line to effluent compositions plotted on arithmetic probability coordinates (Brigham, Reed & Dew 1961; Orr & Taber 1982) or using a one-parameter error minimization similar to that described above for the Coats-Smith model are plotted in Fig. 4.24. Clearly, the dispersion coefficients varied approximately linearly with the average interstitial velocity, as has been observed by others (Perkins & Johnston 1963; Spence & Watkins 1980; Salter & Mohanty 1982). In addition, there was very little difference between the three sandstones. The two straight lines shown have slopes of 1.0 and 1.14. Because solutions to the convection-dispersion equation depend only on the Peclet number, uL/D , approximately linear variation of the dispersion coefficient with velocity produces Peclet numbers and hence solutions which are nearly independent of velocity.

Dispersion coefficients obtained here are consistent with values reported for sandstones by other investigators. Fig. 4.25 compares dispersion coefficients reported by Baker (1977), Spence and Watkins (1980) and Batycky, Maini, and Fisher (1982) with the values reported in Table 4.4. Though there is some range of values at any velocity, it is clear that for the limited number of sandstones studied, differences in dispersive mixing are small.

Table 4.2 Summary of Sandstone Core Properties

Core	Description	Rock Dimensions		Pore Volume cm ³	Porosity %	Air Permeability md	Experimental Dead Volume cm ³	Remarks
		Diameter cm	Length cm					
Berea	Berea Sandstone Outcrop	3.81	15.05	31.7	18.4	180	2.16 ¹ , 0.185 ²	¹ Dead volume for experiment no. 1 ² Dead volume for experiment nos. 2 through 6
B-1	Berea Sandstone Outcrop	3.81	13.9	28.9	18.2	180	0.40	Experiment Nos. 7 through 9
B-1/2	Berea Sandstone Outcrop	1.27	12.07	3.8	25	1000	0.53	Experiment Nos. 10 through 12
B-5/8	Berea Sandstone Outcrop	1.59	22.1	9.25	21.1	500	0.33	Experiment Nos. 13 through 15
F-2	Frannie Reservoir Sandstone	3.81	14.92	34.17	20.1	380	1.1	Experiment Nos. 16 through 18
R-1	Rock Creek Reservoir Sandstone	1.59	21.8	10.55	24.5	--	0.365	Experiment Nos. 19 through 21

Table 4.3 Summary of Carbonate Core Properties

Core	Description	Rock Dimensions		Pore Volume cm ³	Porosity %	Air Permeability md	Experimental Dead Volume cm ³	Remarks
		Diameter cm	Length cm					
H-1	San Andres Dolomite, Seminole	3.81	16.2	33.7	18.2	40	0.85 ¹	¹ Experimental dead volume for experiment nos. 24 through 26. Dead volumes for experiment nos. 22 through 23 are no longer available.
WW-2	San Andres Dolomite, Willard Unit, Wasson Field	1.27	13.7	3.70	21.3	90	0.575	Experiment Nos. 27 through 32
M-1	San Andres Dolomite, Maljamar Field	1.59	31.5	5.67	9.1	6	0.358	Experiment Nos. 33 through 35
SAO	San Andres Dolomite, Outcrop	3.81	66.7	235.16	17	124	1.262	Experiment Nos. 36 through 38

Table 4.4 Summary of Stable, Miscible Displacement Results in Sandstone Cores

Exp't. No.	Core	Average Interstitial Velocity cm/sec	Pulse Size, Pore Volumes	Flowing Fraction	Peclet No. $\frac{uL}{D}$	Dispersion Coefficient cm ² /sec	Damköhler No. $\frac{K_L L}{u}$	Mass Transfer Coefficient sec ⁻¹	Mass Balance Closure $\frac{V_o}{V_{in}}$	Remarks
1	Berea	3.6×10^{-3}	--	1.0	98	5.6×10^{-4}	0	0	0.963	Step input, ethylbenzene/ethylbutyrate, GC composition determination, manual sample collection.
2	Berea	3.8×10^{-3}	--	1.0	100	5.8×10^{-4}	0	0	1.00	" " "
3	Berea	8.7×10^{-3}	--	1.0	102	1.3×10^{-3}	0	0	0.996	" " "
4	Berea	4.8×10^{-3}	--	1.0	87	8.4×10^{-4}	0	0	0.972	" " "
5	Berea	2.0×10^{-3}	--	1.0	148	2.0×10^{-4}	0	0	0.986	" " "
6	Berea	1.3×10^{-3}	--	1.0	155	1.2×10^{-4}	0	0	0.983	" " "
7	B-1	2.6×10^{-3}	--	1.0	90	4.8×10^{-4}	0	0	--	Step input, ethylbenzene/ethylbutyrate, GC composition determination, auto-sample collection.
8	B-1	4.3×10^{-3}	0.5	1.0	79	7.4×10^{-4}	0	0	--	Pulse input, 2%/3% NaCl brine, on-line conductivity cell composition determination.
9	B-1	4.3×10^{-3}	0.5	1.0	78	7.5×10^{-4}	0	0	--	Pulse input, C ₁₀ /C ₁₁ , on-line refractive index composition determination.
10	B-1/2	3.9×10^{-2}	0.55	1.0	62	7.5×10^{-3}	0	0	1.002	" " "
11	B-1/2	3.9×10^{-3}	0.55	1.0	84	5.6×10^{-4}	0	0	0.976	" " "
12	B-1/2	3.9×10^{-2}	0.55	1.0	76	6.2×10^{-3}	0	0	1.029	Pulse input, 2%/3% NaCl brine, on-line conductivity composition determination.
13	B-5/8	3.5×10^{-4}	0.57	1.0	732	1.1×10^{-5}	0	0	0.988	Pulse input, 0.4/0.52% sucrose tracer, on-line refractive index composition determination.
14	B-5/8	3.5×10^{-3}	0.57	1.0	230	3.4×10^{-4}	0	0	0.969	" " "
15	B-5/8	3.5×10^{-2}	0.57	1.0	83	9.05×10^{-3}	0	0	1.011	" " "
16	F-2	3.5×10^{-4}	0.42	1.0	165	3.2×10^{-5}	0	0	1.068	" " "
17	F-2	3.5×10^{-3}	0.42	1.0	140	3.7×10^{-4}	0	0	1.10	" " "
18	F-2	3.5×10^{-2}	0.42	0.974	129	2.8×10^{-3}	$<10^{-4}$	$<10^{-7}$	1.12	" " "
19	R-1	4.6×10^{-4}	0.503	0.998	180	5.5×10^{-5}	0.159	3.3×10^{-6}	0.968	" " "
20	R-1	3.5×10^{-3}	0.503	0.982	236	3.2×10^{-4}	0.076	1.2×10^{-5}	0.985	" " "
21	R-1	3.5×10^{-2}	0.503	0.936	88	8.7×10^{-3}	0.693	1.1×10^{-3}	0.950	" " "

Table 4.5 Summary of Miscible Displacement Results in Carbonate Cores

Exp't. No.	Core	Average Interstitial Velocity cm/sec	Pulse Size, Pore Volumes	Flowing Fraction	Peclet No. $\frac{uL}{D}$	Dispersion Coefficient cm ² /sec	Damköhler No. $\frac{K_m L}{u}$	Mass Transfer Coefficient sec ⁻¹	Mass Balance Closure $\frac{V_o}{V_{in}}$	Remarks
22	H-1	4.4×10^{-3}	0.42	0.687	14.1	5.1×10^{-3}	0.192	5.2×10^{-5}	--	Pulse input, ethylbenzene/ ethylbutyrate, automatic sample collection, GC composition determination.
23	H-1	3.5×10^{-4}	0.42	0.714	13	4.4×10^{-4}	0.155	3.3×10^{-6}	--	" " "
24	H-1	2.6×10^{-2}	0.42	0.658	8.5	5.0×10^{-2}	0.226	3.6×10^{-4}	1.062	Pulse input, 0.4%/0.52% sucrose tracer in Cl ⁻ brine, on-line refractive index composition determination.
25	H-1	2.6×10^{-3}	0.42	0.698	9.9	4.3×10^{-3}	0.119	1.9×10^{-5}	0.939	" " "
26	H-1	2.6×10^{-4}	0.42	0.657	18.1	2.3×10^{-4}	$<10^{-4}$	$<10^{-7}$	0.965	" " "
27	WW-2	2.8×10^{-2}	0.51	0.946	15.4	2.5×10^{-2}	$<10^{-4}$	$<10^{-7}$	1.026	" " "
28	WW-2	2.8×10^{-3}	0.51	0.949	17.6	2.2×10^{-3}	$<10^{-4}$	$<10^{-7}$	1.014	" " "
29	WW-2	2.8×10^{-4}	0.51	0.946	24.9	1.5×10^{-4}	$<10^{-4}$	$<10^{-7}$	0.946	" " "
30	WW-2	2.8×10^{-2}	0.51	0.884	26.9	1.4×10^{-2}	$<10^{-4}$	$<10^{-7}$	1.063	Pulse input, C ₁₀ /C ₁₁ , on- line refractive index composition determination.
31	WW-2	2.8×10^{-3}	0.51	0.897	27.8	1.4×10^{-3}	$<10^{-4}$	$<10^{-7}$	1.024	" " "
32	WW-2	2.8×10^{-4}	0.51	0.880	35.1	1.1×10^{-4}	$<10^{-4}$	$<10^{-7}$	1.051	" " "
33	M-1	4.6×10^{-4}	0.34	0.697	7.0	2.0×10^{-3}	$<10^{-4}$	$<10^{-7}$	1.06	Pulse input, 0.4%/0.52% sucrose tracer in Cl ⁻ brine, on-line refractive index composition determination.
34	M-1	2.5×10^{-3}	0.34	0.621	6.5	1.2×10^{-2}	0.117	9.2×10^{-6}	0.947	" " "
35	M-1	4.6×10^{-3}	0.34	0.561	7.7	1.9×10^{-2}	0.176	2.6×10^{-5}	1.05	" " "
36	SAO	1.6×10^{-3}	--	0.809	21.9	4.8×10^{-3}	0.375	8.9×10^{-6}	0.980	Step input, ethylbenzene/ ethylbutyrate, manual sample collection, GC composition determination.
37	SAO	2.5×10^{-3}	--	0.771	21.7	7.8×10^{-3}	0.395	1.5×10^{-5}	0.954	" " "
38	SAO	6.3×10^{-3}	--	0.766	19.6	2.1×10^{-2}	0.402	3.8×10^{-4}	0.953	" " "

Table 4.6 Summary of Core Properties, Experimental Conditions,
and Results for Core H-1, Two-Phase, Steady-State Displacement

Core Properties

Type: west Texas dolomite
Permeability: ~40 mD
Porosity: 18.2%
Diameter: 1½ inches
Length: 16.2 cm
Pore Volume: 33.7 cc

Experimental Conditions

Experimental Dead Volume: 1.11 cc
 $Q_w = 3.1$ cc/hr
 $Q_o = 0.81$ cc/hr
 $S_w = 0.693$
Total Brine Phase Volume = 23.35 cc
Total Oil Phase Volume = 10.35 cc

Fluids

Oils: n-C₁₀ and 5% n-C₁₁ in n-C₁₀
Brines: 0.4% sucrose and 0.52% sucrose
in 3% mixed brine

Results

Brine Phase:

Fraction Trapped = 0.484 phase PV
 $f = .4708$
 $a = 1.032$
 $Pe = 11.0$
 $D = 1.82 \times 10^{-3}$
 $K_m = 7.9 \times 10^{-5}/\text{sec}$
 $u = 1.24 \times 10^{-3}$ cm/sec (3.51 ft/day)

Oil Phase:

Fraction Trapped = 0.161 phase PV
 $f = 0.8109$
 $a = 0.1928$
 $Pe = 10.76$
 $D = 6.38 \times 10^{-4}$ cm²/sec
 $K_m = 5.0 \times 10^{-6}/\text{sec}$
 $u = 4.2 \times 10^{-4}$ cm/sec (~1.19 ft/day)

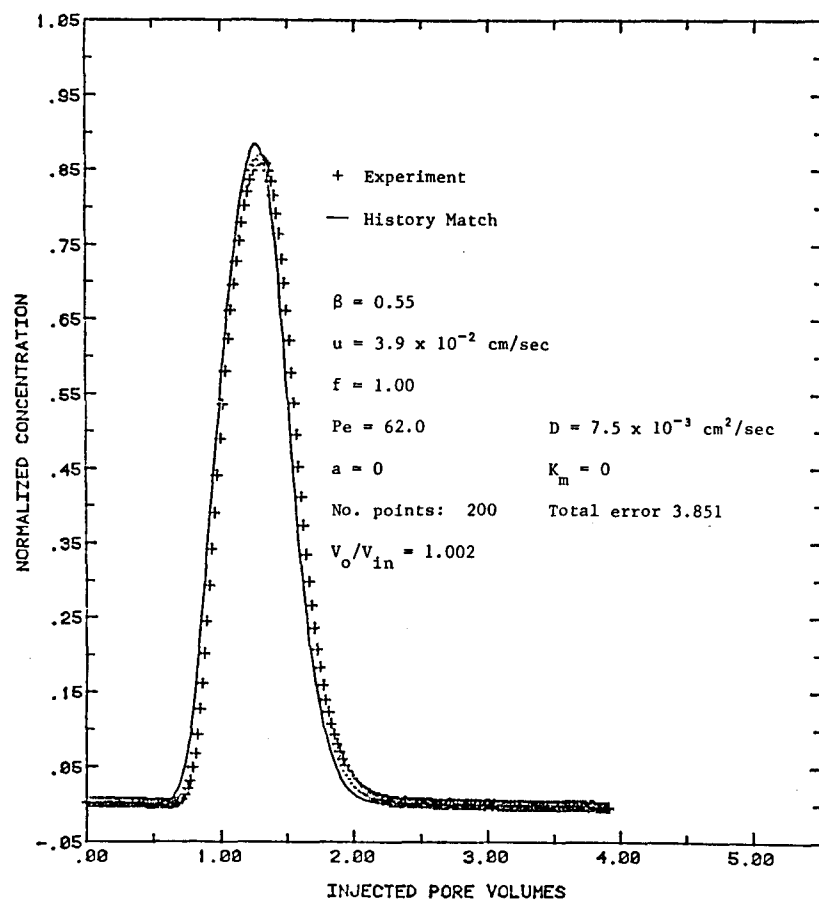


Fig. 4.21 Effluent composition history for displacement no. 10 in a Berea sandstone core (B-1/2).

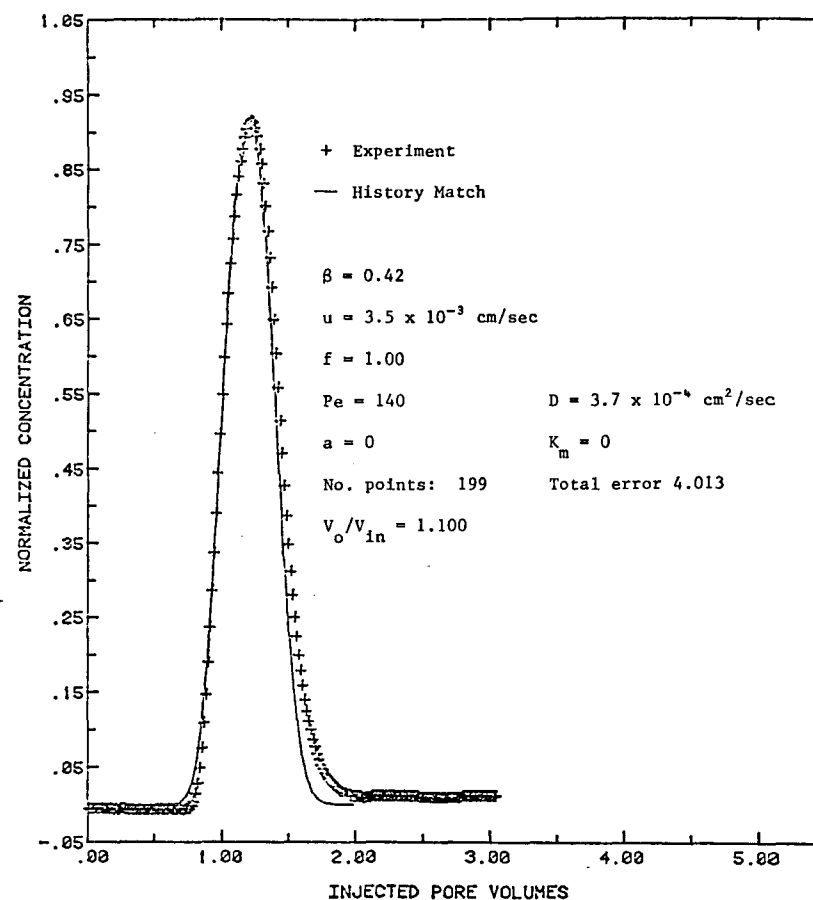


Fig. 4.22 Effluent composition history for displacement no. 17 in a Frannie sandstone core (F-2).

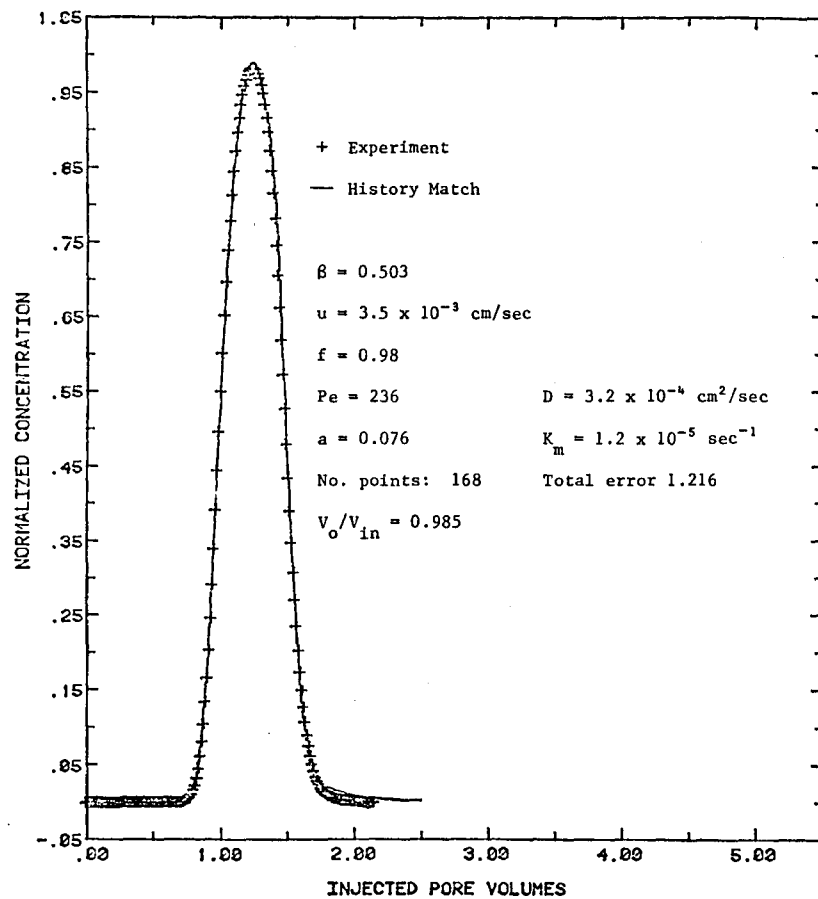


Fig. 4.23 Effluent composition history for displacement no. 20 in a Rock Creek sandstone core (R-1).

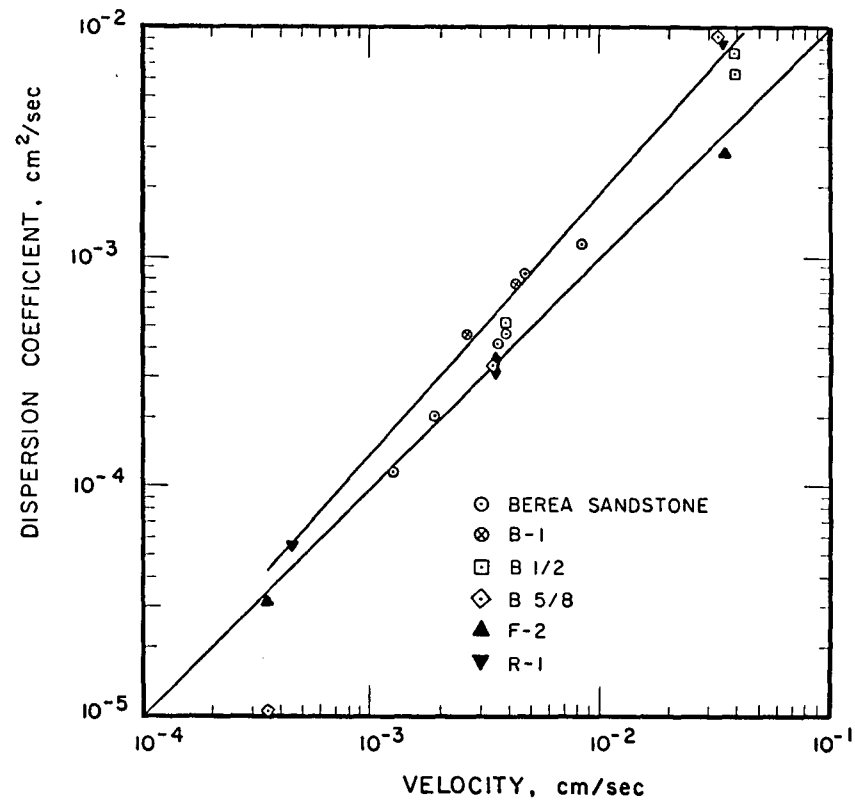


Fig. 4.24 Dispersion coefficients for sandstone cores.

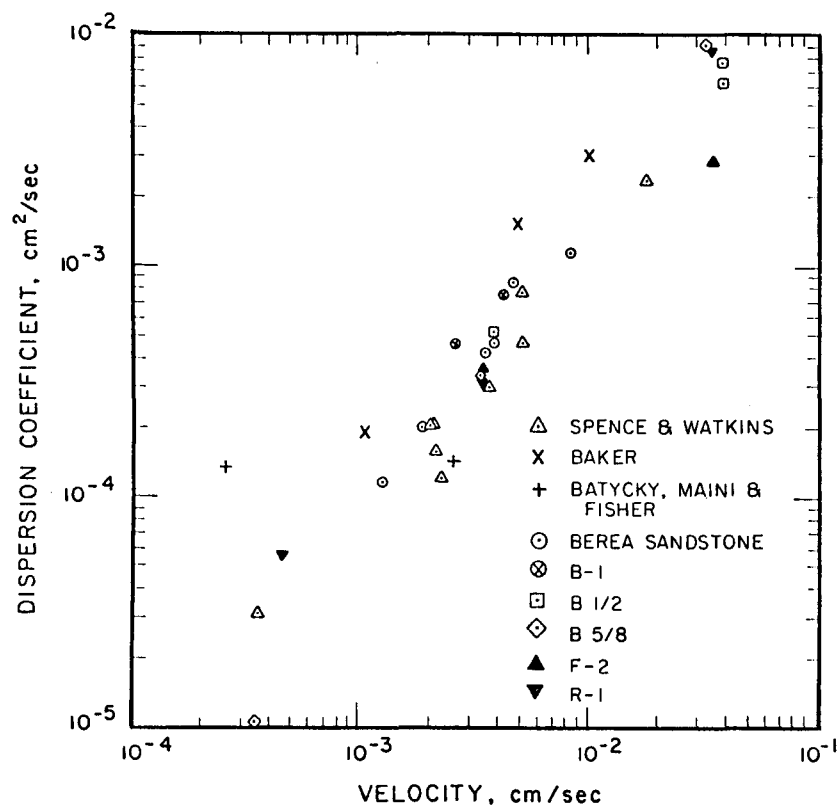


Fig. 4.25 Dispersion coefficients for sandstone cores.

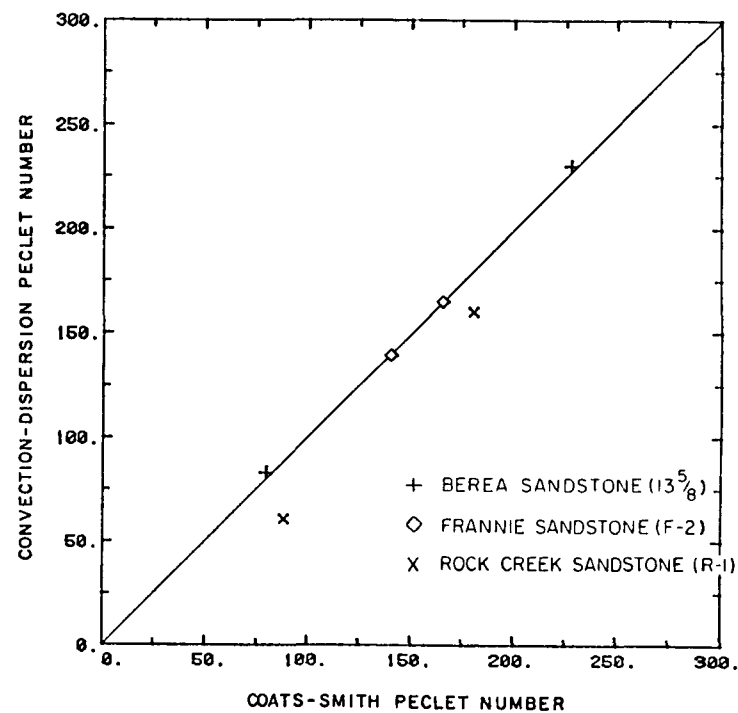


Fig. 4.26 Composition of Peclet numbers estimated using the Coats-Smith model and the convection-dispersion equation for several sandstone core samples.

The behavior of the displacements in the sandstone cores was consistent with the idea that the pore space was relatively uniform (see §4.5). The fact that the 50% concentration appeared at about one pore volume injected suggests that no preferential flow paths were present. To examine the sensitivity of the Coats-Smith model, parameter fits were performed for several of the sandstone displacements, even though they were well modeled by the Peclet number alone. Fig. 4.26 compares Peclet numbers from the two models. Clearly, there was very little difference between the values obtained by the two methods.

Flowing fractions determined with the Coats-Smith model are also given in Table 4.4. All are near one. In most cases, the mass transfer coefficients were very low, though, of course, they are only weakly determined if the flowing fraction is near one. It seems likely that the variations in flowing fraction obtained for the sandstones are a reflection of the precision of the measurement. Small errors in the pump rate, for instance, could lead to errors in the arrival time of the injected pulse. In the current version of the equipment, pump rates are checked directly by weight, but in earlier displacements pump rates alone were used to determine the time scale. Because the flowing fraction is sensitive to the arrival times of the leading and trailing edges of the pulse, small errors in measurements of those times would translate directly into errors in the flowing fraction. Material balance errors, which arise from analytical error or error in the time scale, have a similar effect, because the fitting scheme adjusts the arrival time of the calculated pulse to minimize the error in fitting the leading and trailing edges of pulse largely by adjusting the flowing fraction. The variations in the flowing fraction are of the same magnitude as typical material balance errors, as is indicated in Table 4.4. Thus, most of the flowing fractions obtained do not appear to be sufficiently different from one to justify any conclusions about trends with changes in velocity. They are, however, very different from the values obtained for some carbonate samples.

The one possible exception is the Rock Creek sandstone. Observations of thin sections suggest that a broader pore size distribution and nonuniform distribution of clay minerals might lead to preferential flow paths. See §4.5 for a discussion of the effects of pore structure on mixing.

Single-Phase Displacements: Carbonate Cores

Table 4.5 summarizes results of single-phase displacements in carbonate core samples. Displacements were performed in cores from three fields, Seminole, Wasson and Maljamar, in which CO₂ floods are now underway. Properties of those cores are summarized in Table 4.3. All of those cores were from the San Andres formation, which accounts for considerable production in the Permian basin. Also reported are displacement results for a San Andres outcrop core taken from the Algerita escarpment in northeastern New Mexico.

Figs. 4.27-4.30 give typical effluent composition histories for the four carbonate samples. Similar plots for all of the displacements are included in Appendix B. Three of the four carbonate cores showed significantly earlier breakthrough of injected fluid and more tailing than did the sandstones, as is

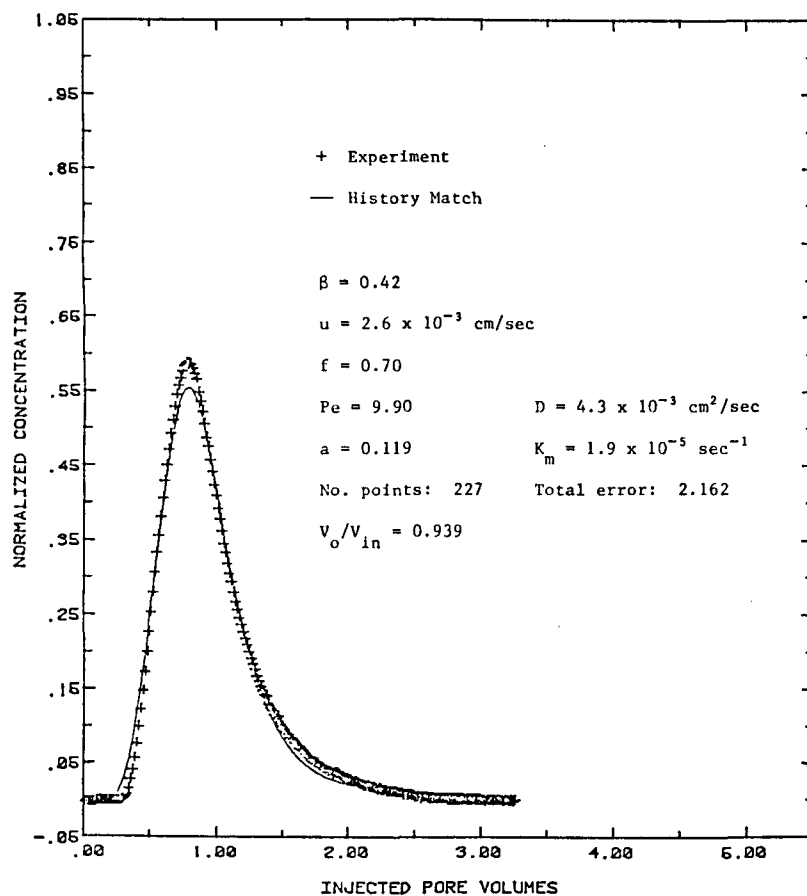


Fig. 4.27 Effluent composition history for displacement no. 25 in a Seminole San Andres core (H-1).

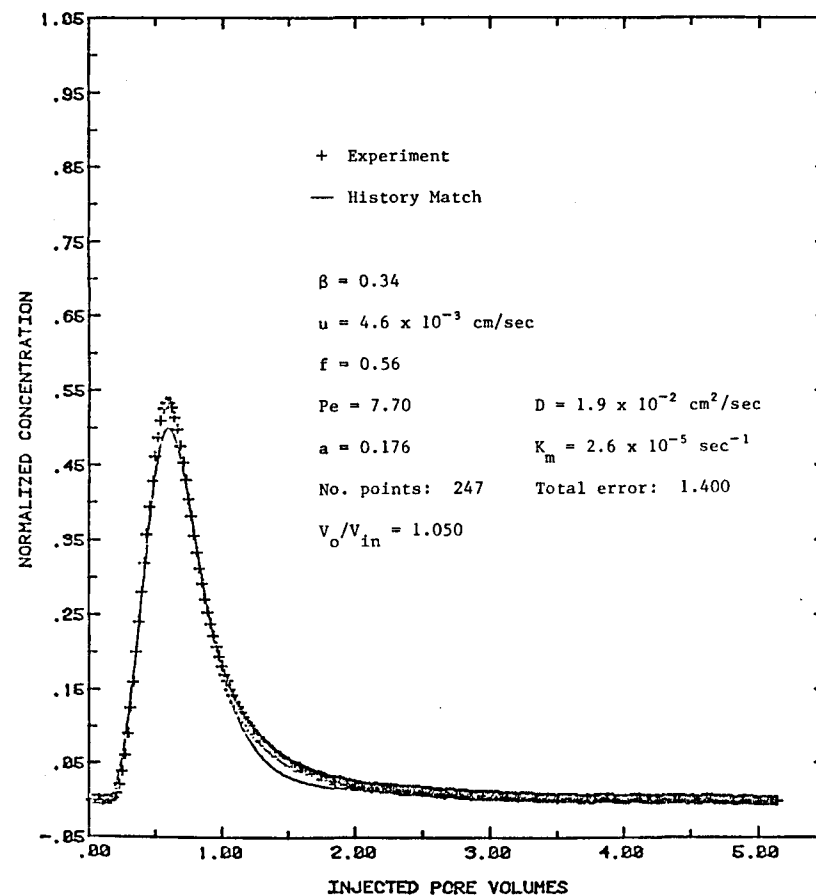


Fig. 4.28 Effluent composition history for displacement no. 35 in a Maljamar core (M-1).

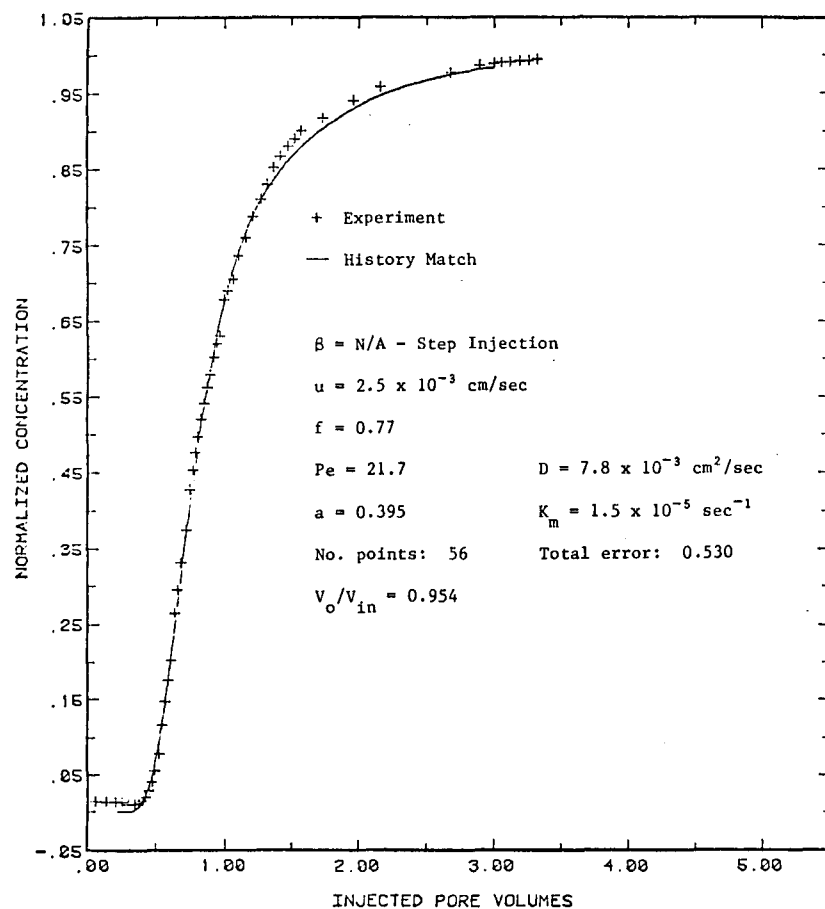


Fig. 4.29 Effluent composition history for displacement no. 37 in a San Andres outcrop core (SAO).

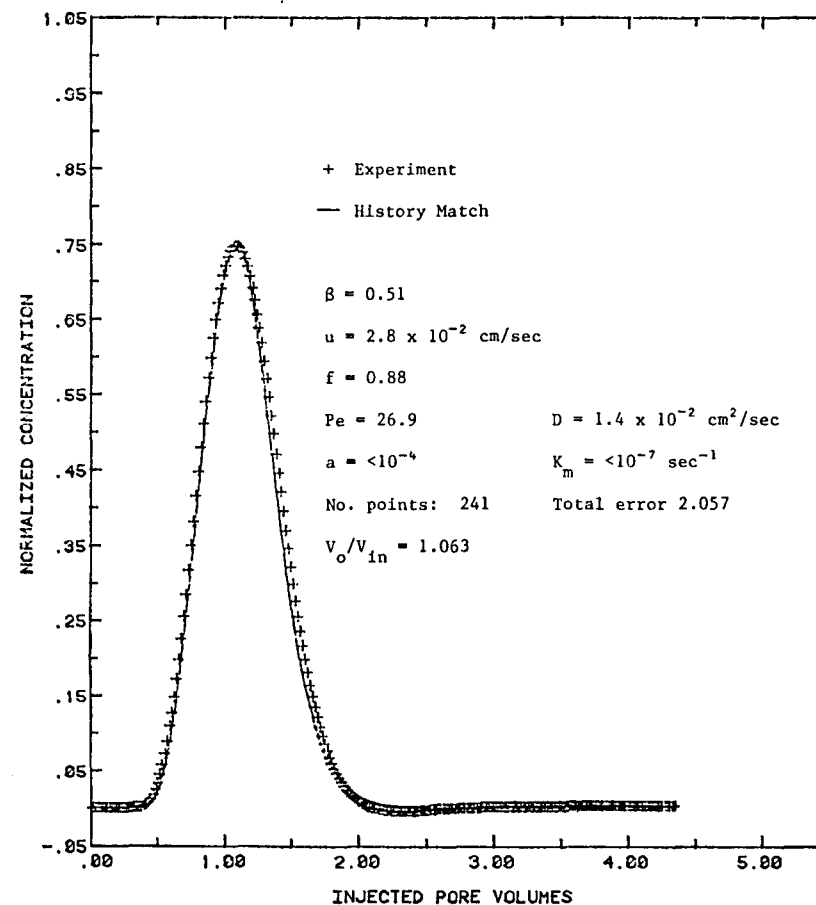


Fig. 4.30 Effluent composition history for displacement no. 30 in a Wasson core (WW-2).

shown in Figs. 4.27-4.29 for displacements in the Seminole, Maljamar and San Andres outcrop cores. The fourth core, from the Willard unit of the Wasson field, showed later breakthrough and a much more symmetric effluent concentration curve. Coats-Smith parameters determined for the four samples reflect the breakthrough pattern. As Fig. 4.31 indicates, the Wasson core showed values of f near one, while values obtained for the other cores were significantly lower: around 0.75-0.80 for the San Andres outcrop core, 0.65-0.71 for the Seminole sample and 0.56-0.70 for the Maljamar sample. Examination of thin sections from the cores revealed significant differences in the pore structures of the different San Andres cores which seem roughly consistent with the flowing fraction data shown in Fig. 4.31. Details of that part of the investigation are reported in §4.5.

Coats-Smith parameters for the Wasson core (WW-2) were determined in two sets of experiments, one with C_{10}/C_{11} mixtures and the other using sucrose as a tracer. In both cases, Coats-Smith parameter fits produced flowing fractions less than one despite the fact that mass transfer coefficients were negligibly small. If the effects of mass transfer were small, then the flowing fraction should have been one. In addition, the flowing fractions determined in the two sets of experiments were different (0.95 and 0.89).

Several possible explanations for the low values of the flowing fractions were investigated. The possibility of non-unique parameter values in the Coats-Smith model was explored by examining fits for wide ranges of initial parameter values. It is sometimes possible to fit the same data with either a high flowing fraction, high dispersion coefficient and low mass transfer coefficient or with a low flowing fraction, low dispersion coefficient and high mass transfer coefficient. Attempts to find a second set of parameters did not succeed for $f > 0.08$. Smaller values of f were not investigated because impractically small time steps would have been required to avoid numerical instabilities in the finite difference scheme used to solve the differential equations of the Coats-Smith model. Even a value of $f = 0.08$ seems physically implausible, however. Thus, non-uniqueness does not appear to explain the results.

Another possibility is that measurement errors in the determination of the core pore volume, end cap dead volume or dead volume of the flow lines downstream of the core caused errors in the time scale of the displacement experiments. When mass transfer is negligible in the Coats-Smith model, the flowing fraction is set by the arrival time of the peak. The arrival time of the peak is set by the core pore volume and the dead volume, which must be subtracted from the produced fluid volume to obtain the time at which a fluid sample left the core. The core pore volume was determined gravimetrically three times, with the three values differing by less than 0.02 cm^3 . Adjustments of the pore volume used in the simulations indicated that better fits were obtained if the measured value was reduced by 2%, which also suggests that error in the core pore volume was not large enough to explain the results. The dead volume in the inlet tube and end caps was only 0.07 cm^3 , so even large percent errors in its measurement would be much too small to account for the problem. If measurement errors in dead volume are the source of the discrepancy, the most likely source is the volume of the valves at the core inlet and outlet. These two valves each have a volume of 0.2 cm^3 .

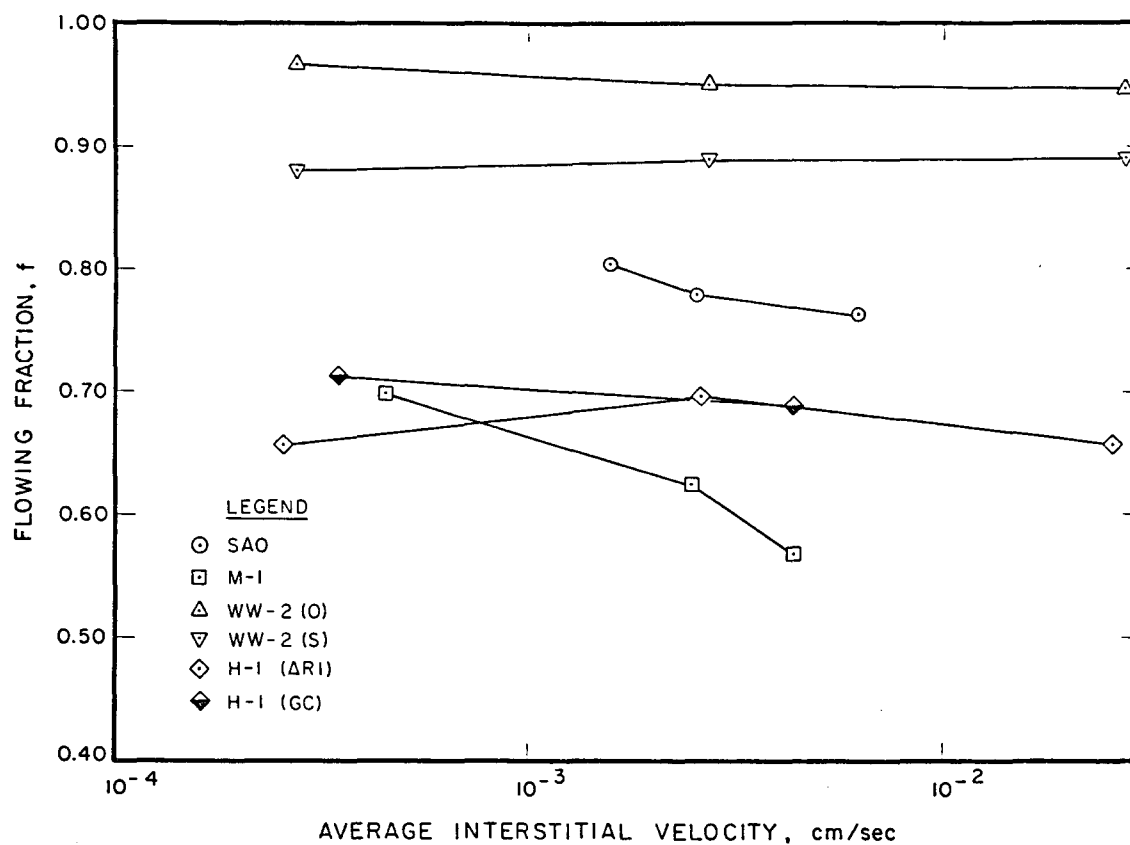


Fig. 4.31 Effect of flow velocity on flowing fraction in carbonate cores.

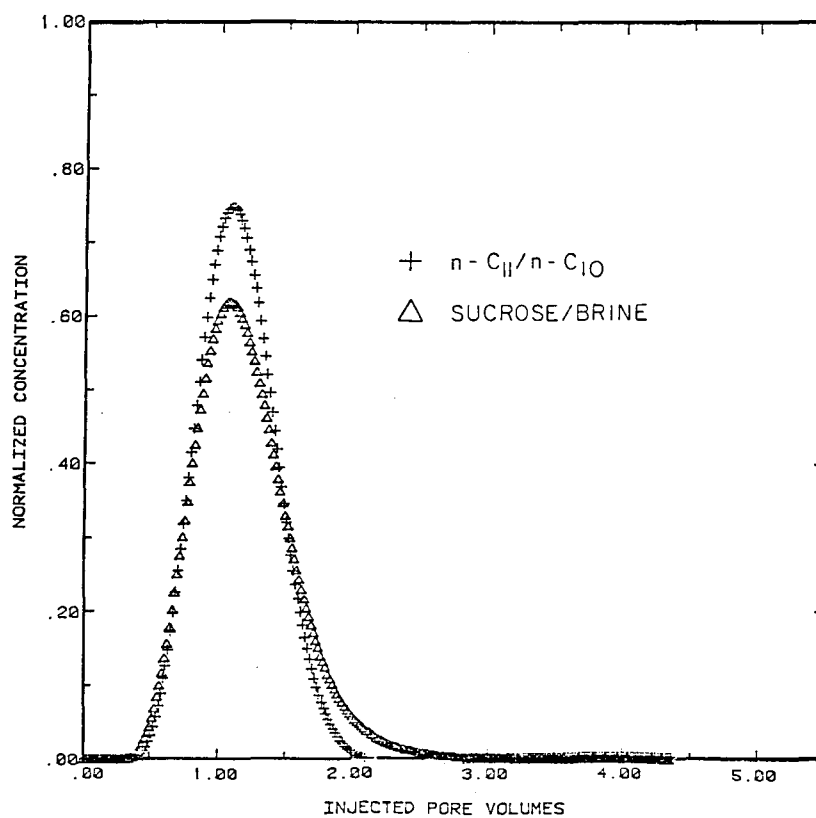


Fig. 4.32 Comparison of displacements (runs 27 and 30) using different tracers in a Seminole San Andres core (H-1).

If the value of the dead volume correction used was too high, the peak concentration would arrive early. Thus, it is possible that if some of the dead volume in the valves was bypassed during the displacement, the peak would appear to arrive early, as was observed. It would not explain, however, why the amount of volume unaccounted for was different in the sucrose-brine and C_{11} - C_{10} displacements.

Two additional possibilities cannot be ruled out. The core in question was cleaned and resaturated a number of times during the course of the experiments described. It is conceivable that a small amount of a second phase, brine or oil, could have been present in the core, removing some of the pore space from flow. It is also possible that undetected errors in setting or recording the pump rates occurred. Any systematic error in the pump rate would shift the arrival time of the peak. After the displacements in question were completed, erratic pump rates due to dirty brushes in the pump motor were detected. In later floods produced fluids were collected on a balance to allow rates to be checked, but it is possible that at the time of the displacements pump errors may have occurred.

Despite the uncertainty concerning the flowing fraction, all the displacement in core WW-2 could be modeled accurately by accounting for the effects of dispersion alone. Dispersion effects did not appear to be the same in the sequences of displacements with different fluids. For example, Fig. 4.32 compares C_{10}/C_{11} and sucrose/brine displacements at 78 ft/day. At all three velocities, peak height was greater and peak width smaller in the C_{10}/C_{11} displacements. As a result, the dispersion coefficients which best fit the effluent compositions were significantly larger for the sucrose-brine displacements than for the C_{11} - C_{10} displacements. Differences in diffusion coefficients probably explain the differences in dispersion coefficients. The diffusion coefficient of C_{11} in C_{10} is estimated to be about $2.7 \times 10^{-5} \text{ cm}^2/\text{sec}^8$ (for comparison C_{12} in C_6 has a value of $2.7 \times 10^{-5} \text{ cm}^2/\text{sec}^9$), and the coefficient for sucrose in water is reported to be $0.52 \times 10^{-5} \text{ cm}^2/\text{sec}^{10}$. In their review paper on dispersion in porous media, Perkins and Johnston (1963) argued that the dispersion coefficient is independent of the diffusion coefficient if the flow is slow enough that diffusion can equalize concentrations within a pore. The ratio of estimates of the time to diffuse a pore diameter to the time to flow a pore diameter is the microscopic Peclet number. For a pore diameter of $300 \mu\text{m}$ (§ 4.5), the Peclet numbers for the sucrose-brine solutions range from 1.6 to 160 while those of the C_{11} - C_{10} mixtures range from 0.3 to 30. Thus, only at the lowest rates are the times for diffusion and flow close to comparable for the sugar solution. At higher rates, the lower diffusion coefficient of the sucrose leads to additional spreading of the transition zones because insufficient time is available for complete mixing at the pore level. Perkins and Johnston (1963) suggested that dispersion coefficients can be calculated as

$$\frac{D}{D_o} = \frac{1}{F\phi} + 0.5 \frac{u \sigma d_p}{D_o} \quad (4.28)$$

where D is the longitudinal dispersion coefficient, D_o the diffusion coefficient, u the average interstitial velocity, σ a heterogeneity factor, d_p

a characteristic particle diameter, ϕ the porosity and F the formation resistivity factor. Perkins and Johnston report that eq. (4.28) is valid as long as $u\phi d_p/D_o < 50$. Spence and Watkins (1980) reported values of ϕd_p for San Andres carbonate samples which ranged from 0.1 to 2.0 cm, and estimated F as 20. If ϕd_p is taken as an intermediate value of 1 cm for the range of velocities considered here, values of $u\phi d_p/D_o$ range from 55 to 5500 for the sucrose solutions and from 14 to 1400 for the C_{11} - C_{10} mixtures. Thus, it is not unreasonable that the dispersion coefficients determined for the two solutions differed.

Dispersion coefficients for all of the carbonate cores are compared with those reported by other investigators in Fig. 4.33. Even with the uncertainty concerning the different values of dispersion coefficients obtained with different fluids, the values reported here fall well within the range of values reported elsewhere. Values obtained for the carbonates were significantly larger than those of sandstones. Dispersion coefficients increased consistently with velocity, and the dependence on velocity was similar to that observed for sandstones. For instance, the dispersion coefficient for core H-1 was approximately proportional to $u^{1.16}$.

Mass transfer coefficients (Fig. 4.34) also fell within the range of values reported by other investigators, and also showed clear increases with average interstitial velocity. Again, the velocity dependence was close to linear. As was the case with sandstones, effluent composition curves changed relatively little with increasing velocity. To produce similar behavior, the Coats-Smith model requires that the flowing fraction and Peclet and Damköhler numbers, uL/D and $K_m L/u$ be nearly constant, which implies that D and K_m are approximately linear in the velocity. Thus, for the limited number of rock samples tested to date, at least, flow velocities can be chosen for experimental convenience and values for other flow velocities obtained from the approximately linear velocity dependence.

Flowing fractions determined for the carbonate samples showed at most only mild dependence on velocity (Fig. 4.30). They were much more consistent than values reported by others (Fig. 4.6). Only the San Andres outcrop and Maljamar samples showed any dependence. For both samples, flowing fractions decreased slightly as the velocity increased. In both samples pore size distributions were quite broad. It is possible that incomplete mixing by diffusion in the largest pores at higher velocities could produce an effect similar to that observed. No detailed analysis of the details of mixing at the pore level in such heterogeneous pore structures has yet been attempted, however.

Two-Phase Displacement Results

Figs. 4.35 and 4.36 report example results for a two-phase displacement in a west Texas dolomite reservoir core sample (core H-1). Table 4.6 summarizes displacement conditions and results. The amounts of brine and oil trapped, or not communicating with the flowing stream, were determined by material balances on the oil and brine originally present in the core. At a brine fractional flow of 0.79 and a water saturation of 0.69, both phases

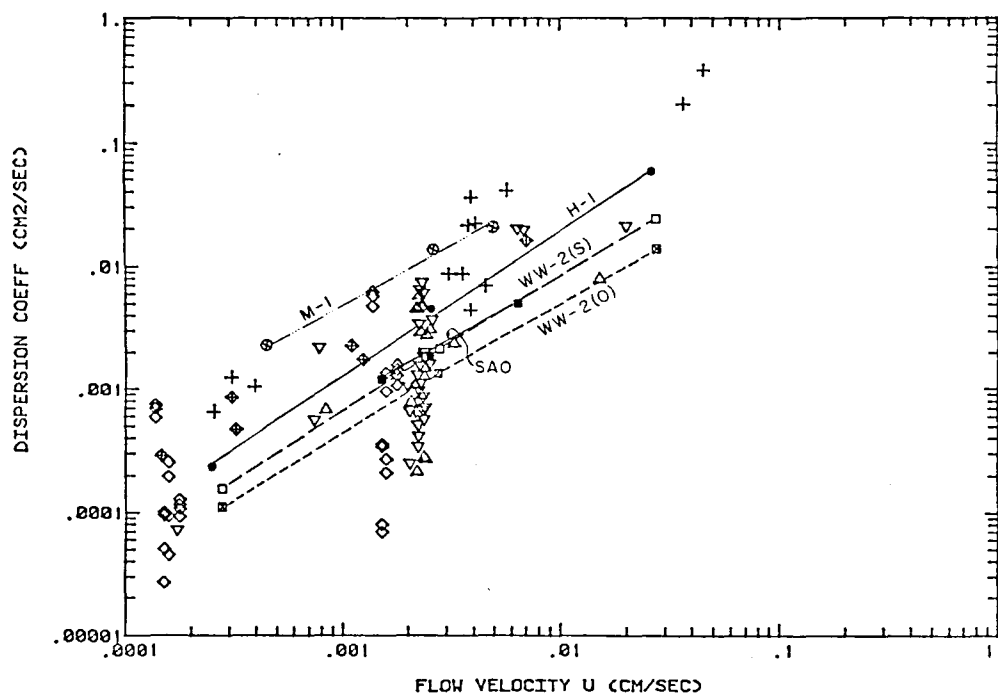


Fig. 4.33 Dispersion coefficients for carbonate core samples. Sources of data: + Batycky, Maini, and Fisher (1982); Δ Spence and Watkins (1980), carbonate A; ∇ Spence and Watkins (1980), carbonate B; \diamond Yellig and Baker (1980); \boxplus Baker (1977); \square Core WW-2 (sucrose tracer); \boxtimes Core WW-2 (C_{10}/C_{11}); \blacksquare Core SAO; \bullet Core H-1; \otimes Core M-1.

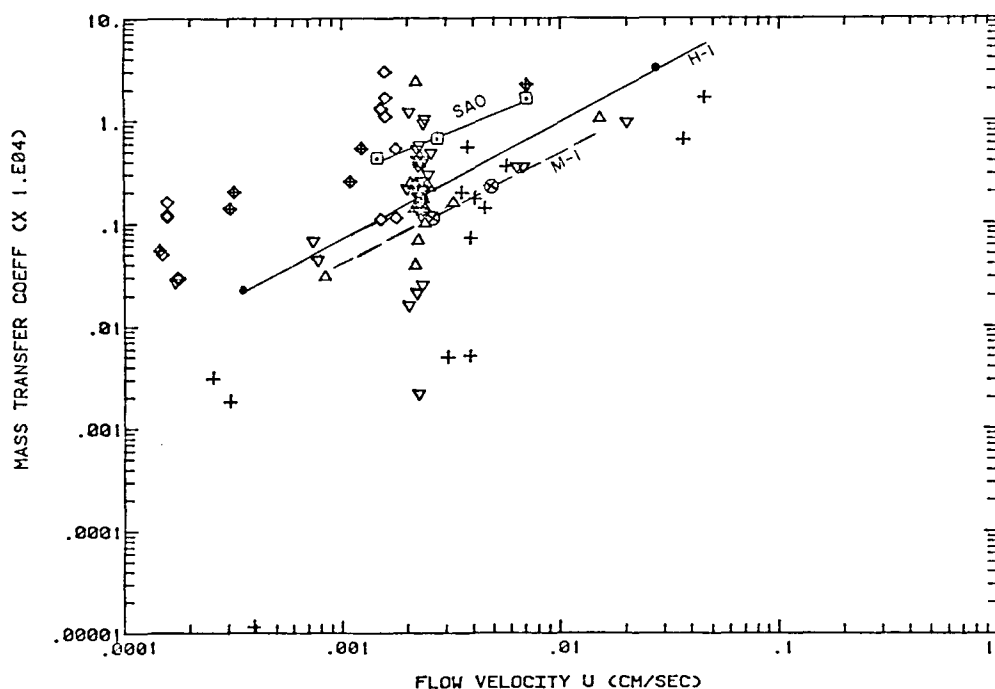


Fig. 4.34 Dependence of mass transfer coefficients on flow velocity for carbonate core samples. Sources of data: + Batycky, Maini, and Fisher (1982); Δ Spence and Watkins (1980), carbonate A; ∇ Spence and Watkins (1980), carbonate B; \diamond Yellig and Baker (1980); \boxplus Baker (1977); \bullet Core H-1; \otimes Core M-1; \boxtimes Core SAO.

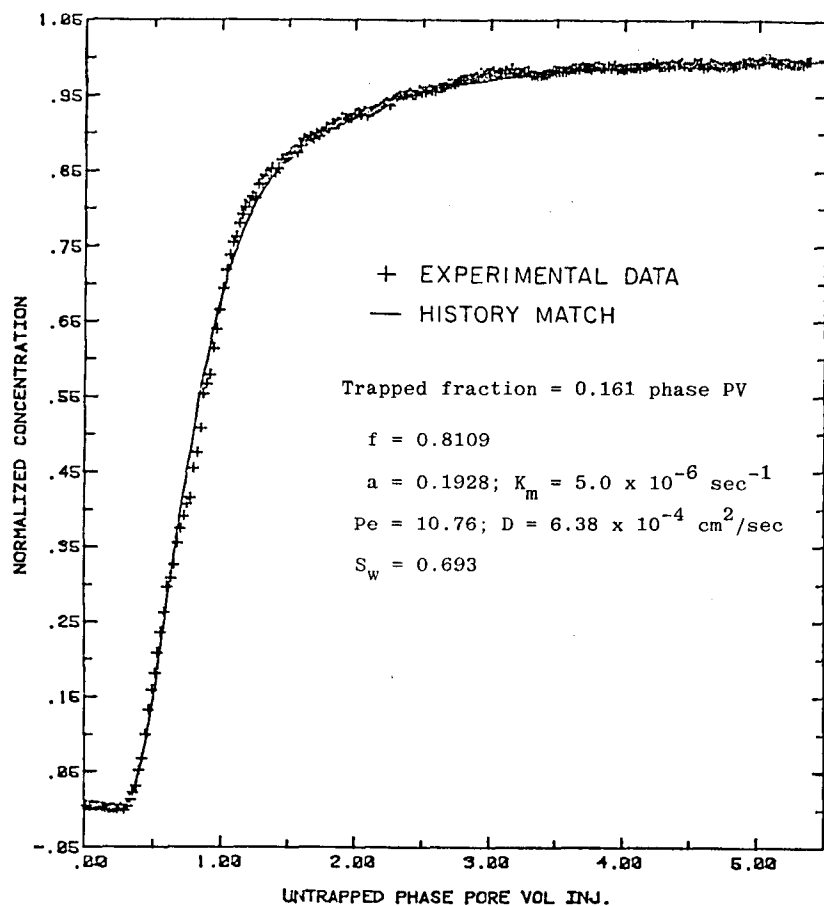


Fig. 4.35 Effluent composition history for the oil phase of a two-phase, steady-state displacement in core H-1, at a brine fractional flow of 0.793 and an oil displacement rate of 1.2 ft/day. Displacement fluids were C_{10} and 5% C_{11} in C_{10} .

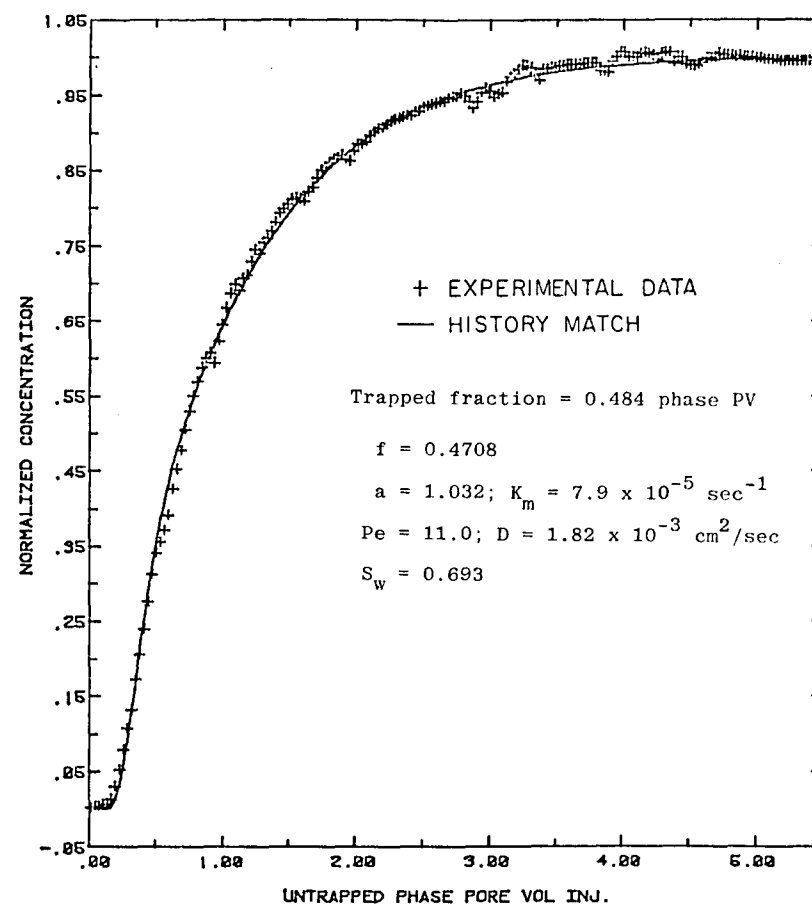


Fig. 4.36 Effluent composition history for the brine phase of a two-phase, steady-state displacement in core H-1, at a brine fractional flow of 0.793 and a brine displacement rate of 3.5 ft/day. Displacement fluids were 3% mixed brines with sucrose as a tracer.

showed significant trapped fractions. The results shown in Figs. 4.34 and 4.35 should be viewed as preliminary. The measurements of trapped saturations are very sensitive to the closure of the overall material balance, and the determinations of the parameters in the Coats-Smith model depend strongly on accurate pump rates, since the time scale for arrival of effluent compositions is based on the volumetric injection rate. To provide a check on the accuracy of the overall material balance and pump rates, the experimental procedure has been modified to allow the collection of all the produced fluids. While details of effluent compositions will still be determined on-line, the material balance can be checked by analysis of the collected fluid. Flow rate can be checked by weighing produced fluids.

Comparison of the Coats-Smith parameters shown in Table 4.5 suggests, however, that the two-phase displacement results are not too unreasonable. The dispersion coefficients in both the oil and brine phases were very close to those determined in the single-phase displacements at the appropriate average interstitial velocity for each phase. Mass transfer coefficients were also roughly consistent with the single-phase results. The oil phase coefficient was very close to that obtained in the single-phase experiment while the water phase coefficient was about 7 times higher. The flowing fractions in the oil and brine phases were 0.811 and 0.471. In all of the single-phase displacements in this core the flowing fraction was in the range 0.65 to 0.70. The two-phase results appear to be consistent with the idea that water occupied the finer pores which probably make up a significant fraction of the dendritic pore space in the single-phase displacements. Thus, the brine phase displacement showed a lower flowing fraction than the average for the whole core. The oil phase, on the other hand, presumably occupied larger pores, more of which are connected to the flowing oil stream, so that the oil phase showed a higher than average flowing fraction. It is harder to rationalize the existence of significant trapped fractions in both phases. Additional experimental work is required to confirm that measurement.

4.5 Analysis of Thin Sections

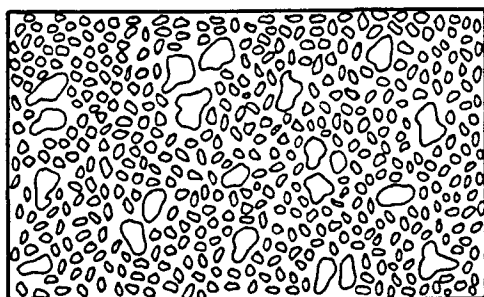
Mixing during flow in a reservoir rock must be strongly influenced by the structure and properties of the pore network. Reservoir rock pore structures, of course, are heterogeneous on scales which range from the pore level to interwell distances. In the discussion that follows we attempt to relate observations of heterogeneities that are visible on the scale of a thin section (20 x 40 mm) to the mixing behavior of single-phase displacements. There are obvious limitations to this approach since there are heterogeneities at larger scales that are not considered at all. It is, however, a first step toward relating flow and mixing behavior to geological structures which occur in reservoir rocks.

In the discussion here we attempt to identify features of the pore space that lead to high or low levels of dispersion and to flowing fractions less than one. In traditional petrophysical analysis of rock pore systems, properties such as porosity, permeability, pore size and shape, and average

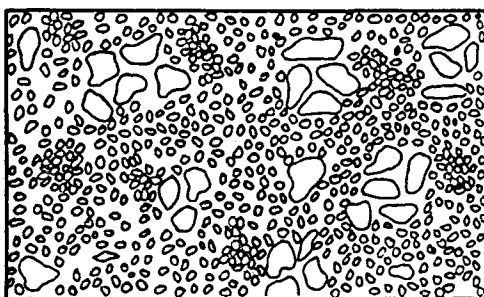
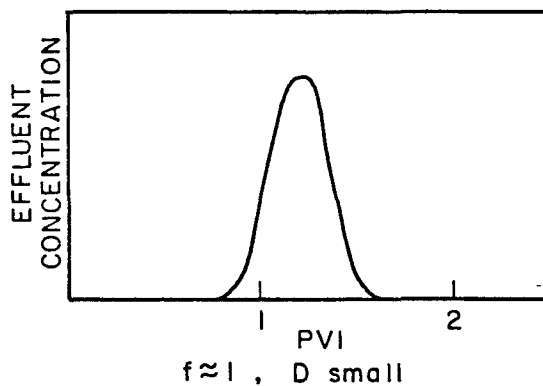
coordination number and aspect ratio are determined. It is not obvious, however, how these properties relate to the sort of averaged mixing observed in the core flood experiments described in §4.4. Individually, none of these properties seems likely to control mixing behavior. It is easy to imagine, for instance, rock samples which have approximately the same porosity and permeability but exhibit totally different mixing behavior. Pore size alone, for the pore sizes typical of many reservoir rocks, seems unlikely to strongly influence mixing. For example, two geometrically similar pore structures differing only in the average size of the pores can be imagined. It seems likely that such samples would produce similar effluent composition histories in miscible displacements as long as the displacement rate was low enough that diffusion could equalize concentrations within typical pores. In displacements in unconsolidated sphere packs, the dispersion coefficient is found to be independent of sphere size for beads larger than almost 30 mesh. Smaller beads show slightly higher dispersion coefficients. Such behavior is usually attributed to difficulties in obtaining uniformly sized particles and uniform packings when the particles are small (see Perkins & Johnston 1963 for references on this point). Pore shape must also play some role in the mixing of miscible fluids, but if pores are, on average, small enough that diffusion can equalize compositions within them, it is not obvious that rectangular pores, say, would produce displacement results very different from those of circular pores. Studies of unconsolidated packs of particles other than spheres suggest that larger dispersion coefficients are obtained for nonspherical particles than for spheres, but the effect is not large (Perkins & Johnston 1963). Aspect ratio, the ratio of pore body to pore throat diameters, and coordination number, the number of other pores connected to a given pore, strongly affect displacement performance when capillary forces are important (Wardlaw & Cassan 1978; Wardlaw 1980; Chatzis et al 1983), but it is not clear how they influence mixing in miscible displacements.

One property which clearly does influence mixing is the pore size distribution. Perkins and Johnston report that several investigators found that dispersion coefficients for sphere packs increase as the width of the particle size distribution increases. Spence and Watkins (1980) found that flowing fractions less than one occurred for rock samples with wide pore size distributions. It seems likely, however, that a wide distribution of pore sizes alone does not guarantee that the flowing fraction is less than one. For instance, Fig. 4.37 shows three idealized pore systems with the same pore size distribution which would have very different mixing behavior. In Fig. 4.37a, the large and small pores are randomly distributed. Flow in such a pore system would be characterized by a flowing fraction of one and a dispersion coefficient higher than that of a totally uniform set of pores but still relatively low. In Fig. 4.37b, pores with the same distribution of sizes are distributed in clusters of small and large pores, but the clusters themselves are randomly distributed so that there are no preferential flow paths for large samples compared to the average length over which clusters correlate. Such a pore system would still have a flowing fraction of one because the local variations in flow would average out over a large enough flow distance. The dispersion coefficient would be larger, reflecting the broader transition zone which would result from the local flow variations.

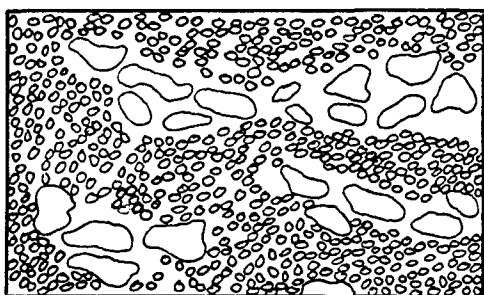
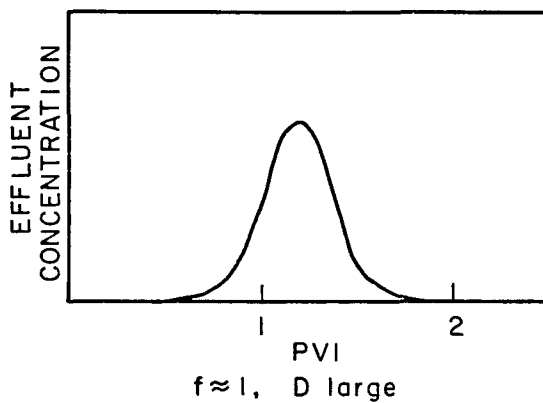
In Fig. 4.37c, a second pore system with clusters of large and small



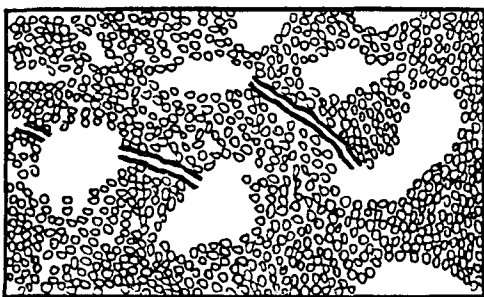
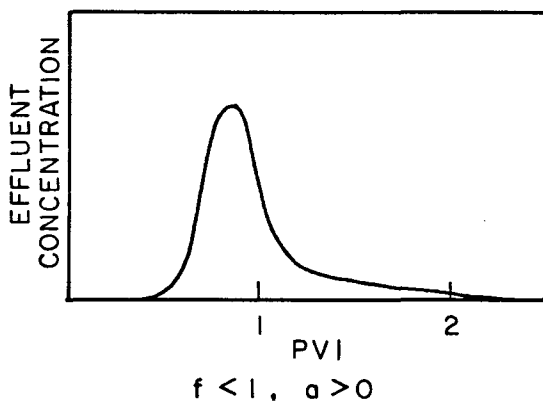
a. RANDOM DISTRIBUTION OF LARGE AND SMALL PORES



b. RANDOM DISTRIBUTION OF CLUSTERS OF LARGE AND SMALL PORES



c. NONRANDOM DISTRIBUTION OF CLUSTERS OF LARGE AND SMALL PORES



d. FRACTURES AND VUGS

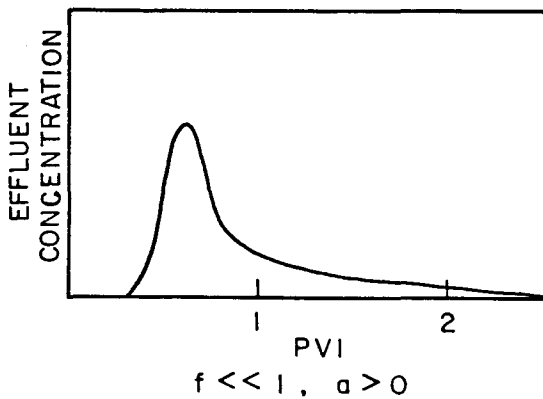


Fig. 4.37 Idealized pore structures.

pores is shown. In this one, however, the distribution of clusters is not random. Preferential flow paths exist and the combination of slower flow in the small pores and diffusive exchange between the small and large pores leads to effluent compositions which can be described by a flowing fraction less than one, dispersion in the flowing stream and mass transfer between a stagnant and flowing stream. The last idealization, shown in Fig. 4.37d, is a pore system containing fractures, vugs and small matrix pores. Again, this sort of pore structure leads to early breakthrough of injected fluid and hence to a flowing fraction less than one. It comes closest to the idealization envisioned in the Coats-Smith model.

The variations in pore structure discussed here can all be lumped under the name microscopic heterogeneity. If the simple qualitative discussion given here is correct, the nature of the heterogeneity also matters. A relatively wide pore size distribution appears to be necessary but not sufficient to produce flowing fractions less than one. The pore space must also be connected in ways which produce preferential flow paths.

In the discussion that follows, we attempt to relate observations of thin sections to the simple qualitative models presented. Thin sections were examined for the seven cores in which single-phase displacements were performed (Figs. 4.38-4.45). Pore body sizes were measured as the diameter of the smallest circumscribed circle around a pore. This definition exaggerates the diameter and volume of the pore somewhat, because it is based on the longest dimension of a pore. Measurement of pore sizes in thin section partly compensates for the exaggeration because a random slice through a rock shows only a few pores which have been cut through their longest dimension. For the qualitative discussion here, any consistent definition is probably adequate. Approximately 300 randomly selected pores were measured for each thin section. The resulting pore size distributions are reported as the percent of total porosity contained in pores of a given size. Porosity was estimated based on the area of circles of the pore diameters divided by the total area.

The distribution of pore sizes for Berea sandstone core B-1 is shown in Fig. 4.38. Fig. 4.46 is a photograph of a portion of one of the thin sections of that material. Pore sizes in this relatively uniform sandstone are distributed in a single, narrow mode. Pores smaller than 80 μm are mostly intergranular pore throats, elongated passages which connect larger and more irregular pore bodies. Small (10-25 μm) crystals of aluminosilicates (clay minerals) line some of the pore walls, and patches of dolomite cement are sparsely distributed around some of the sand grains. Both precipitates appear to be randomly distributed and present in amounts small enough that they offer no significant restriction to flow.

The Frannie sandstone (Figs. 4.39 and 4.47) is very similar to the Berea material in both pore shape and genetic type. The principal differences between them are the smaller grain sizes, and therefore, pore sizes, and the lack of clay mineral precipitates in the Frannie. Observations of the thin sections are summarized in Table 4.7. Also reported in that table are values of the flowing fraction, dispersion coefficient and mass transfer coefficient obtained in the single-phase displacement experiments discussed in §4.4. The values shown are for the displacements at about 10 ft/day (3.5×10^{-3} cm/sec).

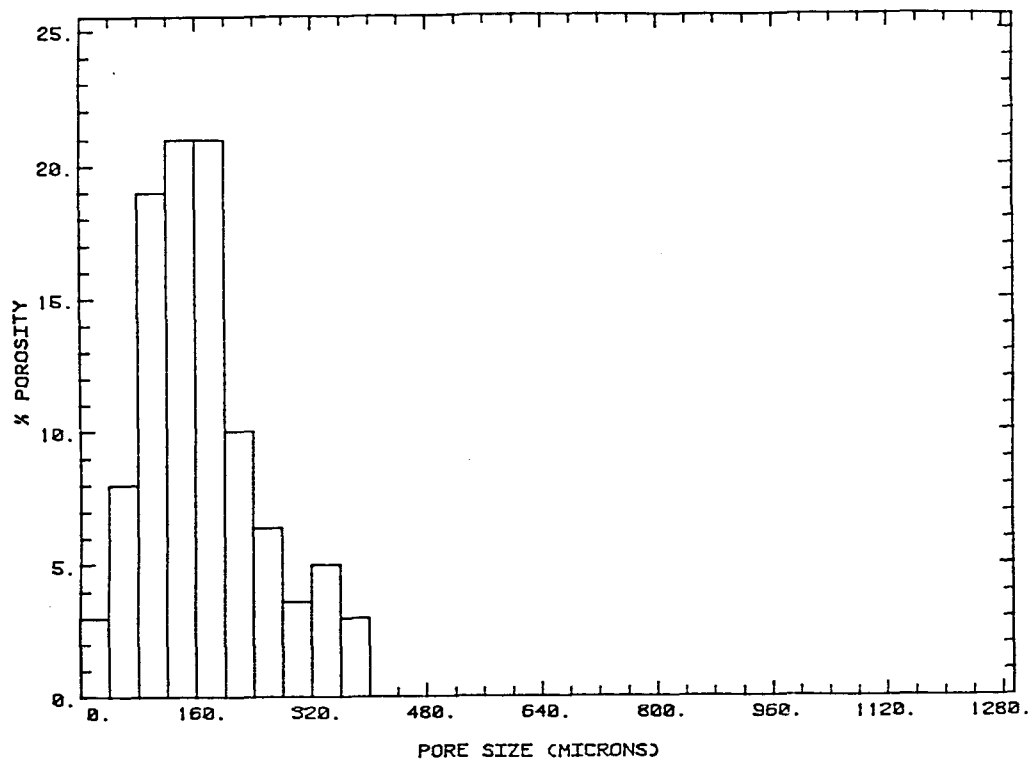


Fig. 4.38 Distribution of pore body sizes for Berea sandstone core B-1.

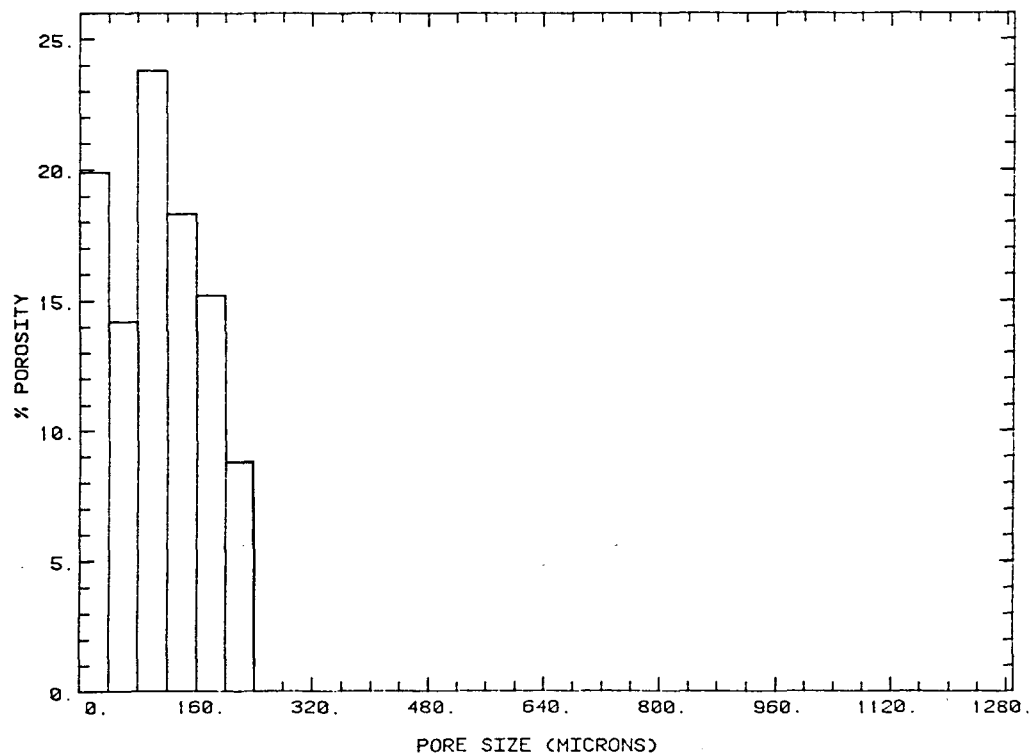


Fig. 4.39 Distribution of pore body sizes for Frannie sandstone core F-1.

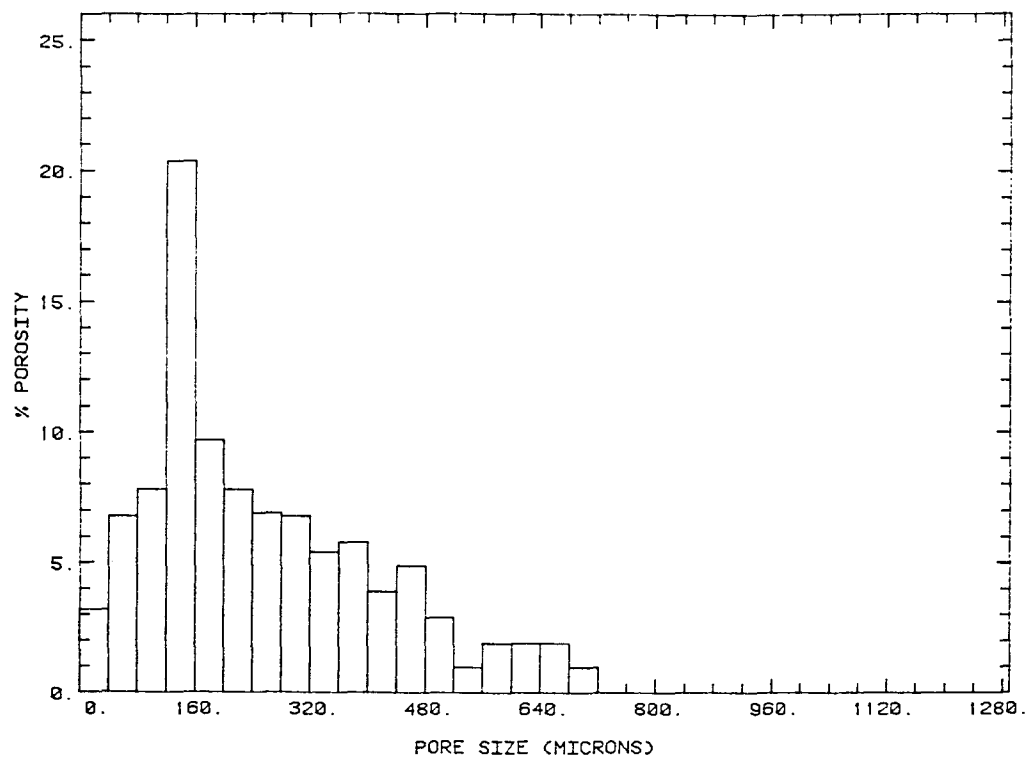


Fig. 4.40 Distribution of pore body sizes for Rock Creek sandstone core R-1.

CO₂-83-114

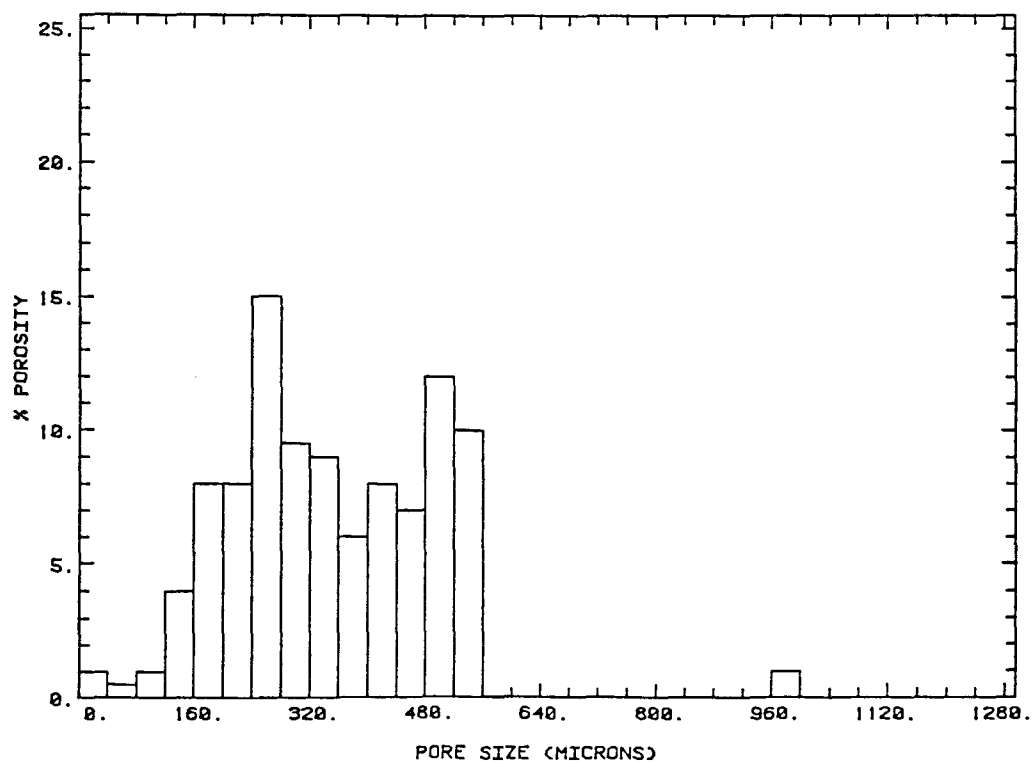


Fig. 4.41 Distribution of pore body sizes for Wasson core WW-2.

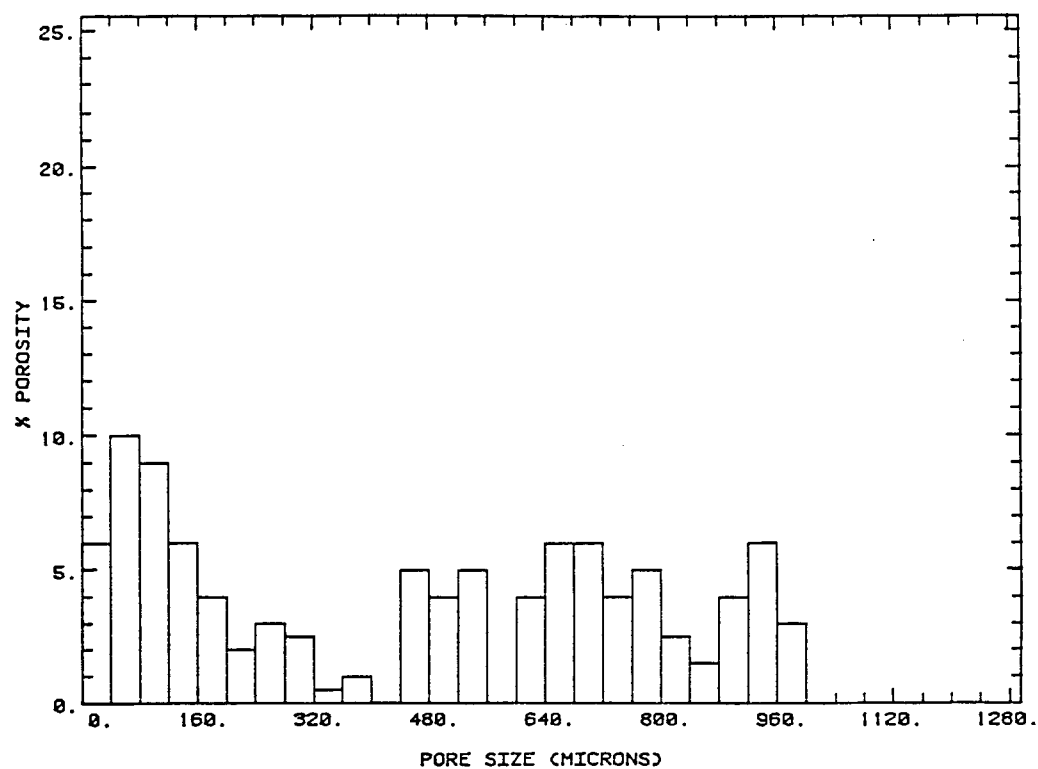


Fig. 4.42 Distribution of pore body sizes for Seminole core H-1.

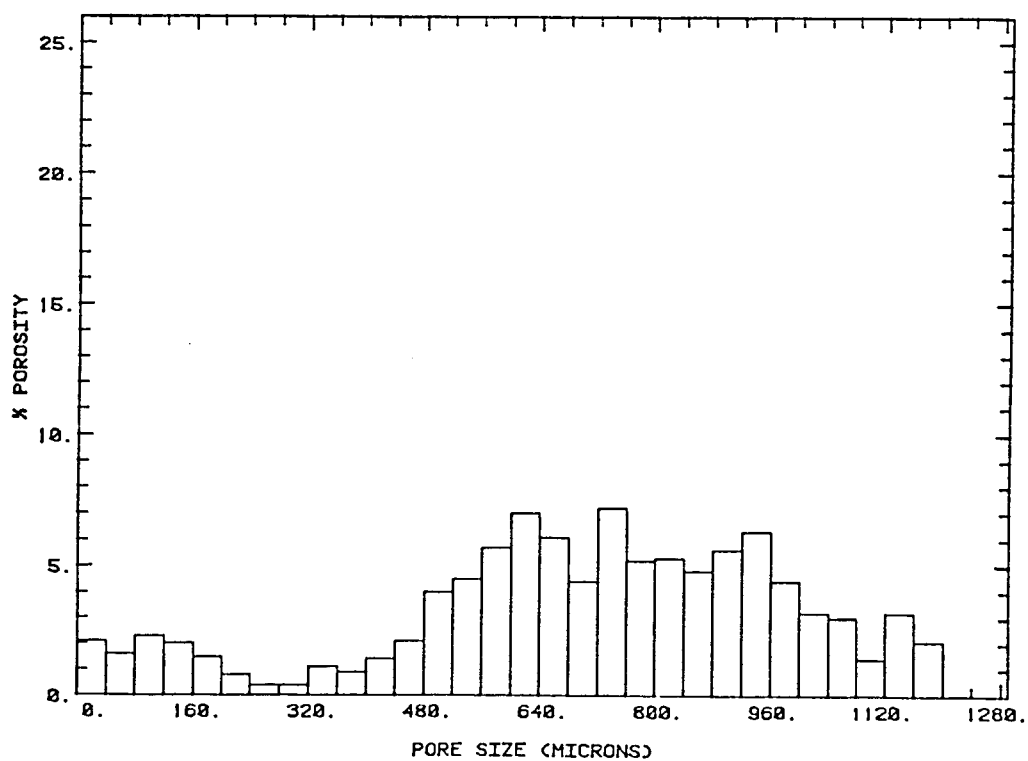


Fig. 4.43 Distribution of pore body sizes for San Andres outcrop SA0.

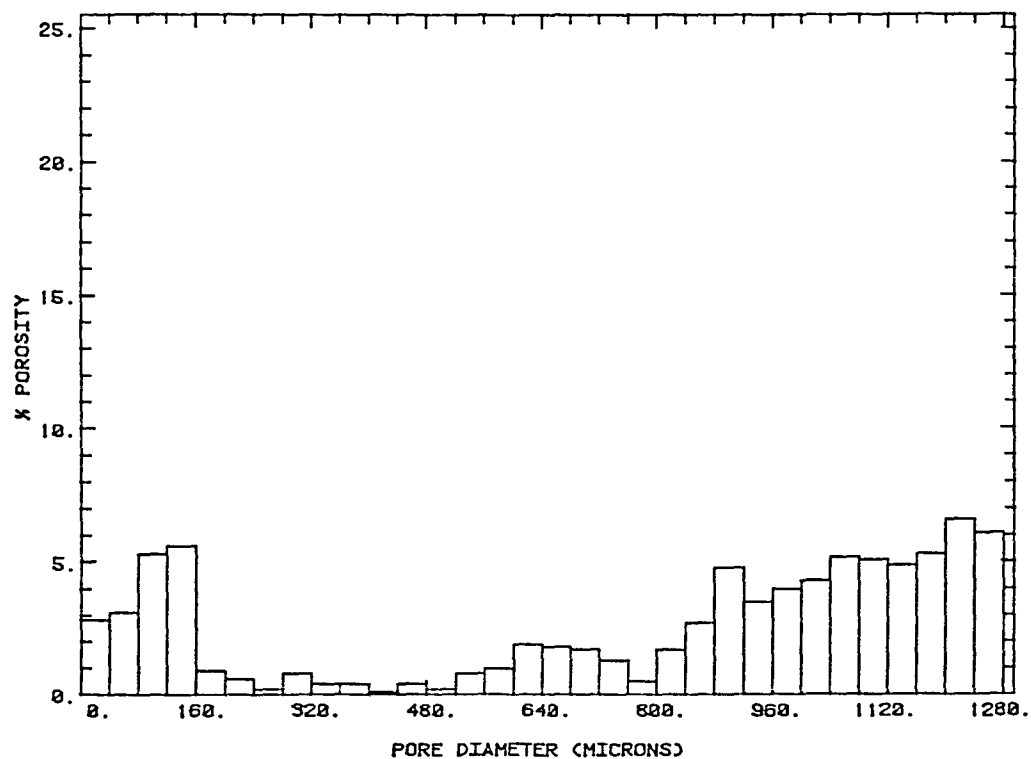


Fig. 4.44 Distribution of pore body sizes for the lower 84% of porosity for Maljamar core M-1.

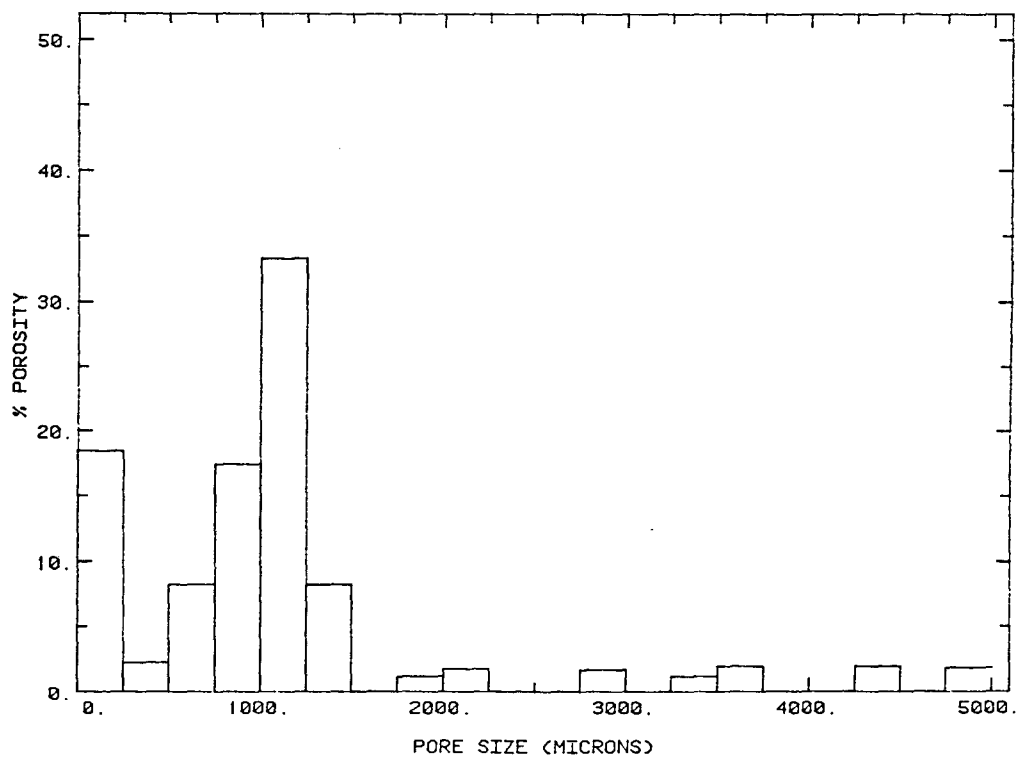


Fig. 4.45 Distribution of pore body sizes for Maljamar core M-1.

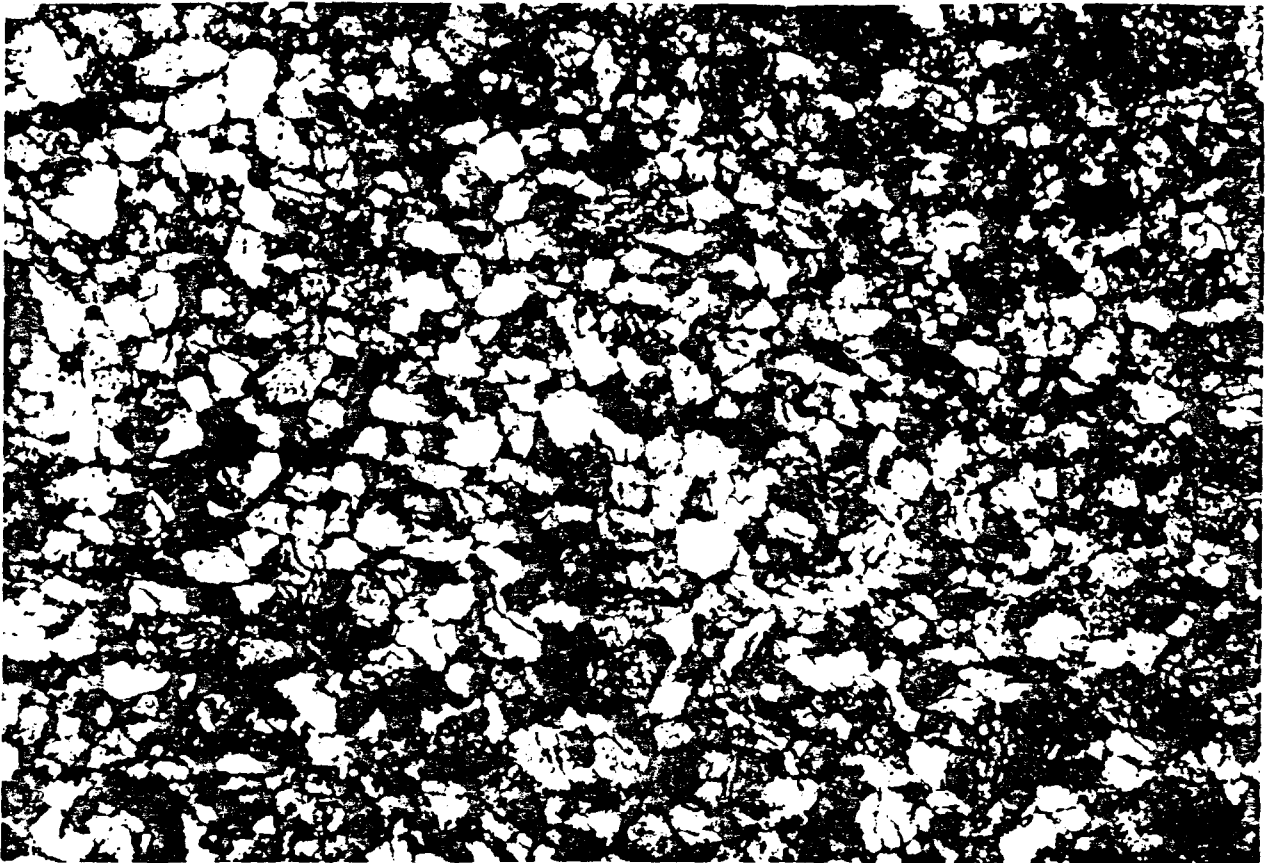


Fig. 4.46 Thin section of Berea sandstone core B-1 (25x). Porosity is black.

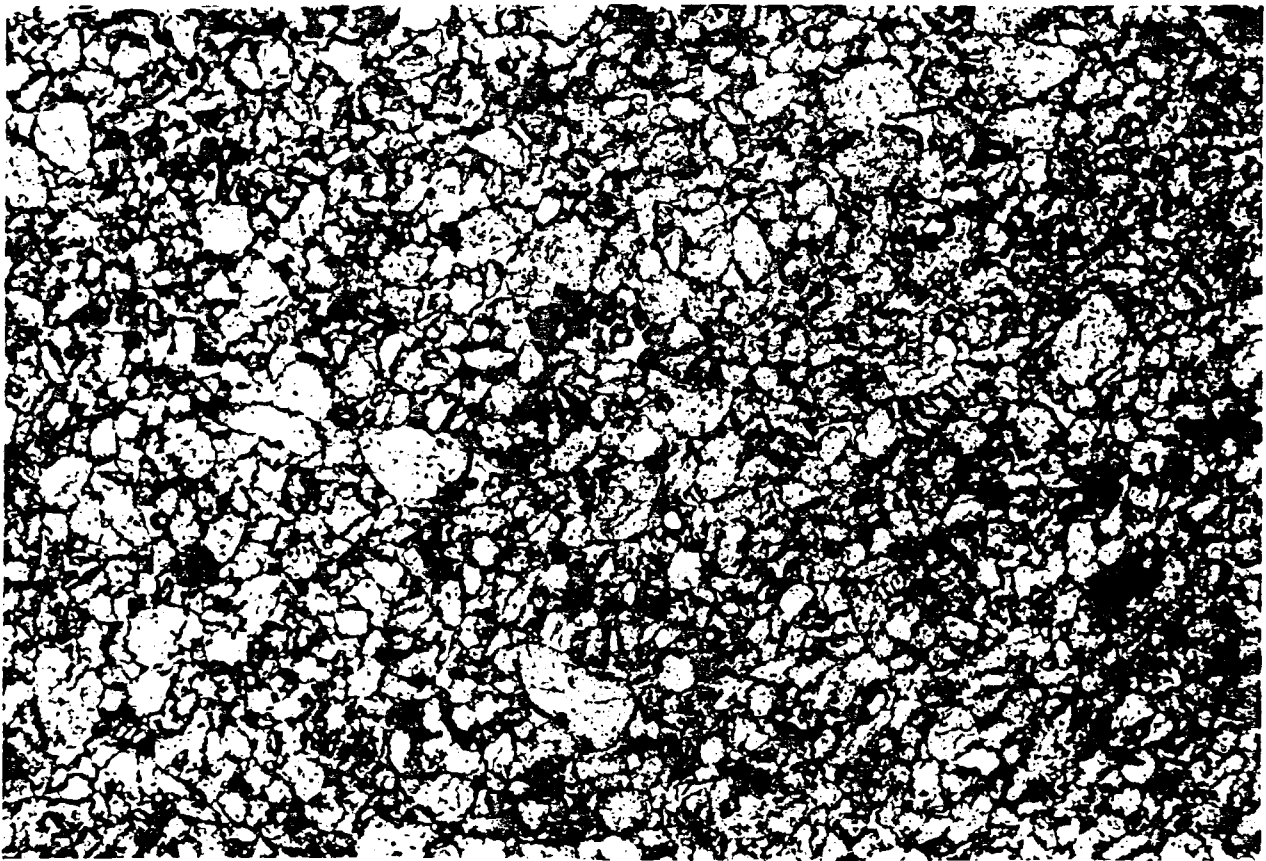


Fig. 4.47 Thin section of Frannie sandstone core F-1 (25x). Porosity is black.

Table 4.7 Description of Thin Sections

Sample	Pore Size Distribution		Non-Random Permeability Barriers	Preferential Flow Paths	Pore Type	Exp't. No.	f	D cm ² /sec	K _m sec ⁻¹
	# Modes	Mean ±Std. Dev. (μm)							
Berea SS (B-1)	One	169.44 ± 83.24	None	None	G	9	1.0	7.5 x 10 ⁻⁴	0
Frannie SS (F-2)	One	108.48 ± 62.98	None	None	G	17	1.0	3.7 x 10 ⁻⁴	<10 ⁻⁷
Rock Creek SS (R-1)	One	259.80 ±165.62	Clay mineral pods (matrix)	Flow through type-G pores around clay pods	G	20	0.982	3.2 x 10 ⁻⁴	1.2 x 10 ⁻⁵
Wasson DM (WW-2)	One	343.23 ±129.42	Minor anhydrite plugging	None	SC	31	0.897	1.4 x 10 ⁻³	<10 ⁻⁷
Seminole DM (H-1)	Three	129.55 ± 90.95 500.00 ± 33.81 786.19 ±117.19	Anhydrite plugging	Flow through vugs indirectly connected by type-C pores	SC,V	22	0.687	5.1 x 10 ⁻³	5.2 x 10 ⁻⁵
San Andres FM (SAO) DM	Two	110.74 ± 66.60 769.84 ±200.81	Type-C pores arranged in spherical clusters	Flow through well-coordinated type-SG and type-V pores	C,SG,V	37	0.771	7.8 x 10 ⁻³	1.5 x 10 ⁻⁵
Maljamar DM (M-1)	Many	Widest distribution of sizes	Preponderance of type-C pores, anhydrite plugging	Flow through fracture/stylolite-connected vugs	C,V,F,M	34	0.621	1.2 x 10 ⁻²	9.2 x 10 ⁻⁶

Key to Pore Types:

C = Inter-crystalline <25μm
 F = Fracture/Stylolite
 G = Intergranular
 M = Moldic
 S = Solution Enhanced (Prefix)
 V = Vugular

In the displacements for the Berea and Frannie sandstones (see Figs. B.9 and B.17), symmetric effluent concentration histories were obtained and the displacements were modeled reasonably well by a flowing fraction of one and a dispersion coefficient. Thus, the pore structures in the Berea and Frannie sandstones appear to be qualitatively similar to that idealized in Fig. 4.37a.

In contrast, the Rock Creek sandstone (Figs. 4.40 and 4.48) has a substantial matrix (~20%) of clay minerals and micaceous laths which are distributed as coherent masses or "pods" around quartz grains. These pods appear to be nonuniformly distributed at the thin section scale. The clay minerals within these permeability barriers are tightly woven together, and may limit access of flowing fluids to a portion of the pore space. The pore size distribution is also broader (Fig. 4.40), additional evidence of microscopic heterogeneity in the Rock Creek sample. As is shown in Table 4.6 (and in Table 4.3), some indication of flowing fractions less than one was found in the displacement experiments at the higher velocities (see also Fig. B.20). Such behavior may have been due to relatively less efficient diffusional mixing between pores containing clays at the higher velocities. Thus, it appears that the more complex pore structure of the Rock Creek sandstone sample could account for the observation of flowing fractions slightly less than one.

The carbonate samples examined showed much greater variation than did the sandstones. Figs. 4.41 and 4.49 show the pore size distribution and thin section photograph for the Wasson core. The pore size distribution for the Wasson material was not greatly different from the Rock Creek material, as the average pore sizes and standard deviations given in Table 4.6 indicate. In fact, the pore size distribution was also similar to that of the Berea core. Pores in the Wasson material appeared to be more nearly spherical than they did in the Berea sample, probably because the dolomitization and subsequent dissolution of carbonate material during diagenesis transformed the original carbonate materials of the sediments. No clays were observed, but some anhydrite was present, particularly in pores with diameters greater than 200 μm . The anhydrite did not fill the pores, but appeared in thin section as small patchy areas. The apparent uniformity of the pore structure of the Wasson material was reflected in the displacements in that core (see Fig. B.31). All were described well by a dispersion coefficient only, even though flowing fractions less than one were obtained (see §4.4 for a discussion of possible explanations for that observation). In any case, both displacement data and thin sections indicate that from the standpoint of mixing, the Wasson core material behaved much more like the sandstones than like the other carbonate samples.

Pore size distributions and a photograph for the Seminole core material are shown in Figs. 4.42 and 4.50. Figs. 4.43 and 4.51 give the same data for the San Andres outcrop sample. Both samples showed much broader distributions of pore sizes than the sandstones or Wasson material. In the San Andres outcrop sample, there was considerable interparticle porosity due to extensive dissolution of cements and grains. Also present in the San Andres outcrop material were ooid grains within which small intraparticle pores were observed. The pore space within the ooid grains was surrounded by low permeability, fine crystalline dolomite. Presumably, flow into and out of

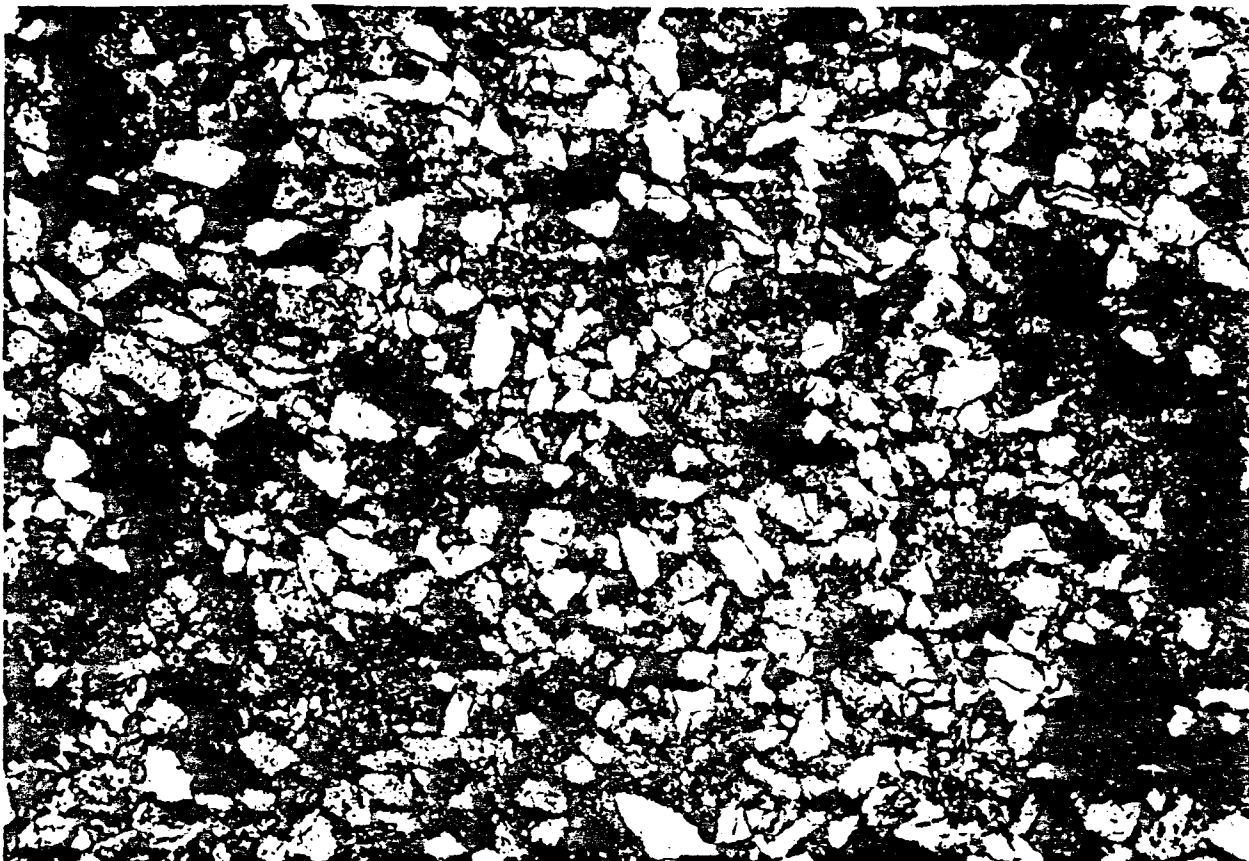


Fig. 4.48 Thin section of Rock Creek sandstone core R-1 (25x). Porosity is black.

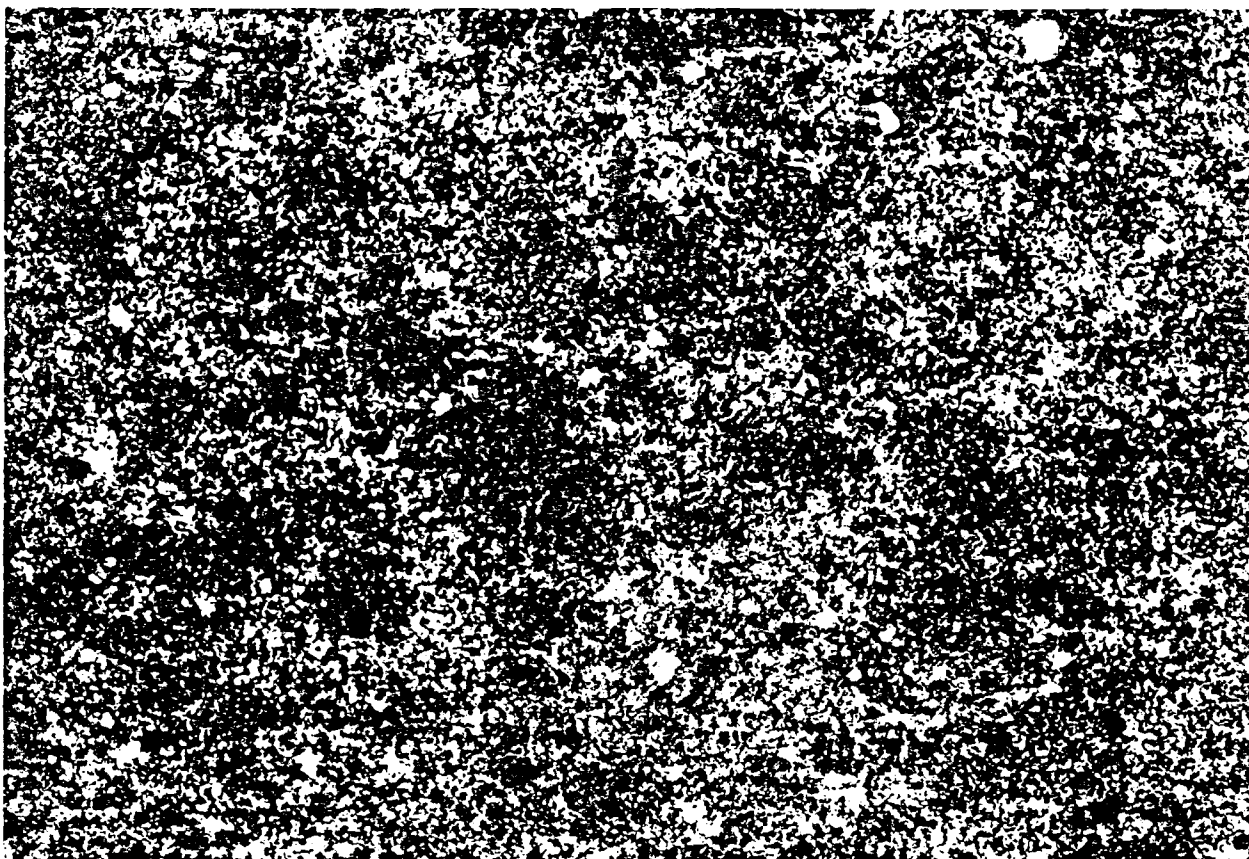


Fig. 4.49 Thin section of Wasson San Andres core WW-2 (25x). Porosity is black.

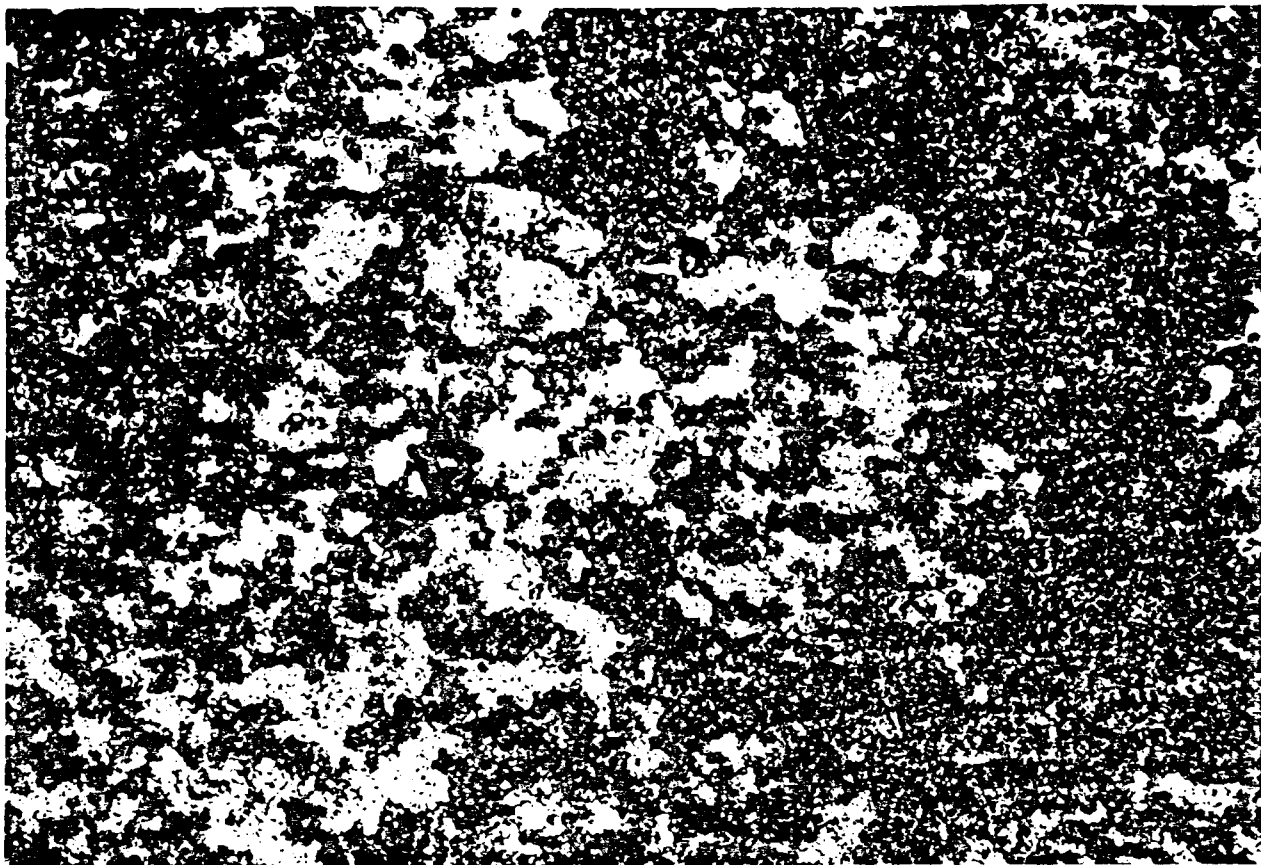


Fig. 4.50 Thin section of Seminole San Andres core H-1 (25x). Porosity is black.

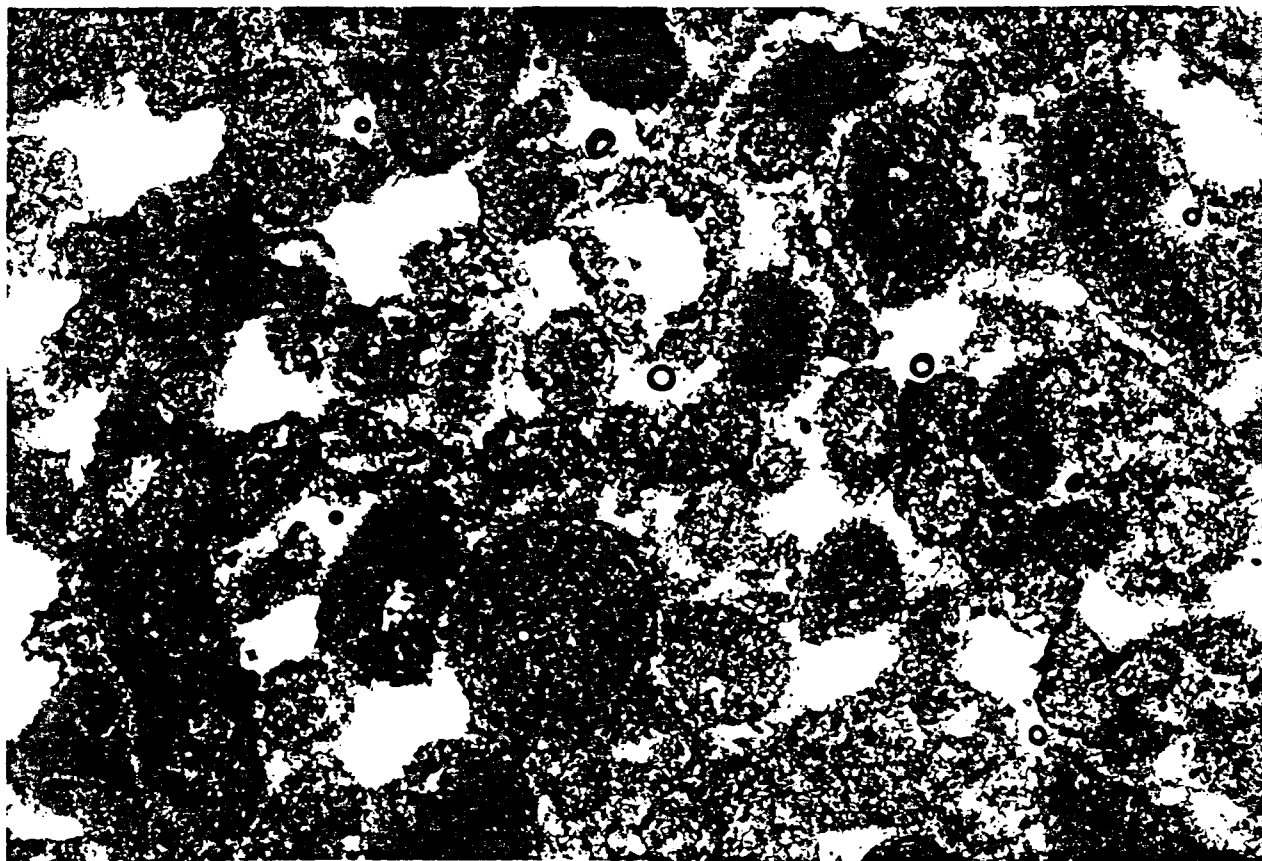


Fig. 4.51 Thin section of San Andres outcrop core SAO (25x). Porosity is white.

such pore space was much slower than in the well connected interparticle pore space. Thus, fluid in the ooid grains would exchange with fluid in the preferential flow path by slow flow and diffusion. Thus, that sample appears to be similar to the idealization of Fig. 4.37c: a wide pore size distribution with pore connections that generate preferential flow paths. It showed a flowing fraction much less than one, a large dispersion coefficient and a significant mass transfer coefficient in displacement tests (Tables 4.6 and 4.5, and Fig. B.37).

The Seminole core material showed similar displacement behavior, but the details of the pore structure observed in thin section were significantly different. Extensive recrystallization of the carbonate material apparently obliterated the original ooids, leaving a dolomite fabric containing many small pore and some medium size and large pores (Figs. 4.42, 4.50 and B.22). A significant fraction (31%) of the pore volume was in pores with diameters less than 160 μm . The larger pores appeared to be connected to each other or located with only small zones of smaller pores between them. Thus, it appears that preferential flow paths could have been present. Flow in the small matrix porosity must have been much slower. Some anhydrite was observed to block some pores of intermediate size, and may have further restricted access of flowing fluid to the matrix in some portions of the pore space. Thus, the Seminole material also appears to fit the idealization of Fig. 4.37c, but with pore geometry different from that of the San Andres outcrop sample.

Samples of Maljamar dolomite (core M-1) exhibited the widest pore size distribution of the cores examined in this study (Figs. 4.44 and 4.45). The rock is composed of tightly woven euhedral to anhedral dolomite crystals. Seventeen percent of the pore space consists of intercrystalline voids with diameters less than 25 μm (Fig. 4.52). Large vugs directly connected by fractures and stylolites dwarf the surrounding intercrystalline micropores (Fig. 4.53). Most of the porosity was in very large vugs (Fig. 4.45). The fact that at least some of the vugs were connected by fractures must have generated preferential flow paths, and exchange of fluid between those flow paths and the fine matrix porosity must have generated the long tail observed in the displacement experiments (Fig. B.34). The Maljamar core showed the earliest breakthrough and hence the lowest flowing fraction of any of the cores tested. Thus, this sample is similar to the idealization of Fig. 4.37d. It seems clear from the observations of thin sections of the Maljamar core material that the displacement behavior is consistent with features of the pore structure present in the thin section.

Throughout the discussion here, two aspects of microscopic heterogeneity have been considered. The first is a distribution of pore sizes. If the distribution of pore sizes is broad, early breakthrough may occur, but only if the pore space is also connected in ways that generate preferential flow paths. Microscopic fractures, solution pores through fine matrix porosity and no doubt other pore structures, can generate such flow paths. Qualitative observations of thin sections appear to be consistent with displacement behavior in stable, single-phase miscible displacements. In multiphase displacements, the distribution of phases within the pore structure must also influence mixing. Wetting behavior will control the distribution of phases between small and large pores and hence must also affect mixing. Thus, the

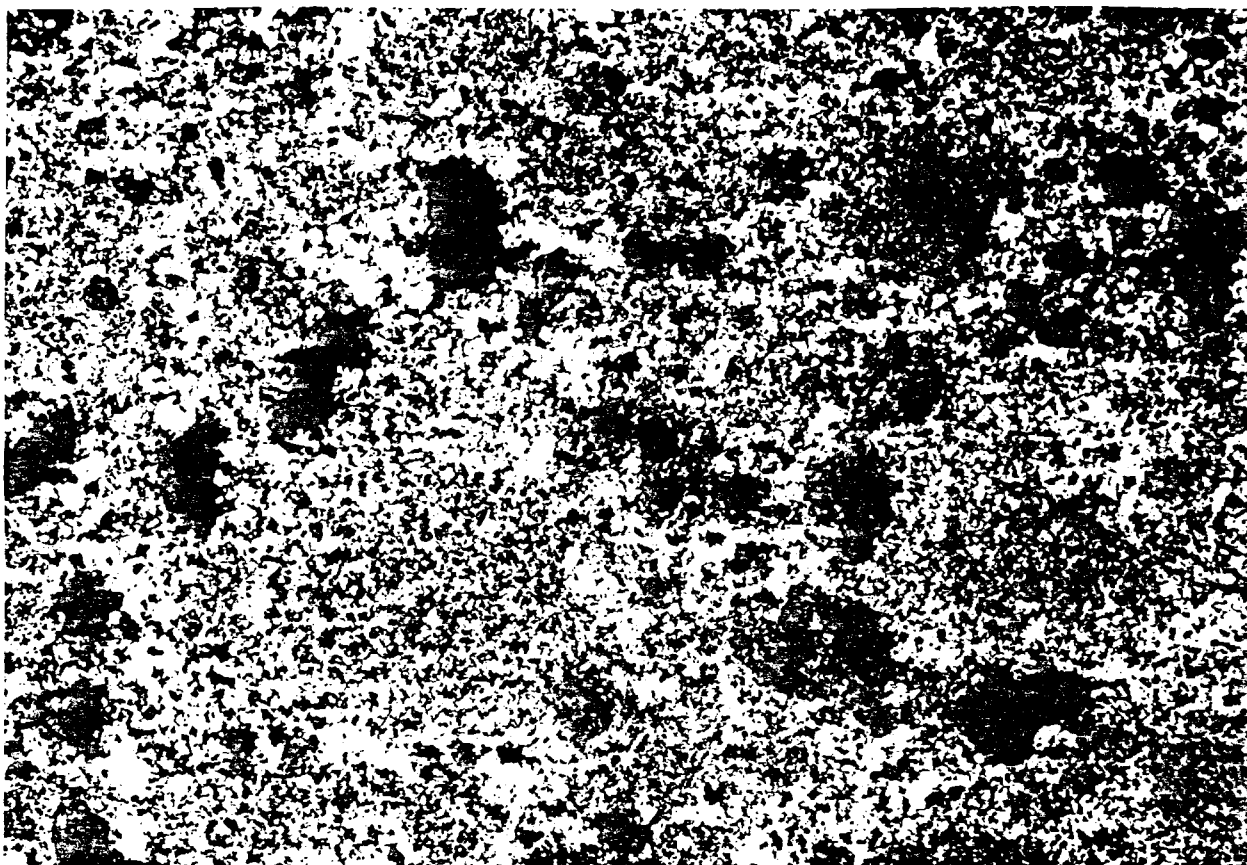


Fig. 4.52 Thin section of Maljamar San Andres core M-1 (25x) showing matrix porosity. Porosity is black.

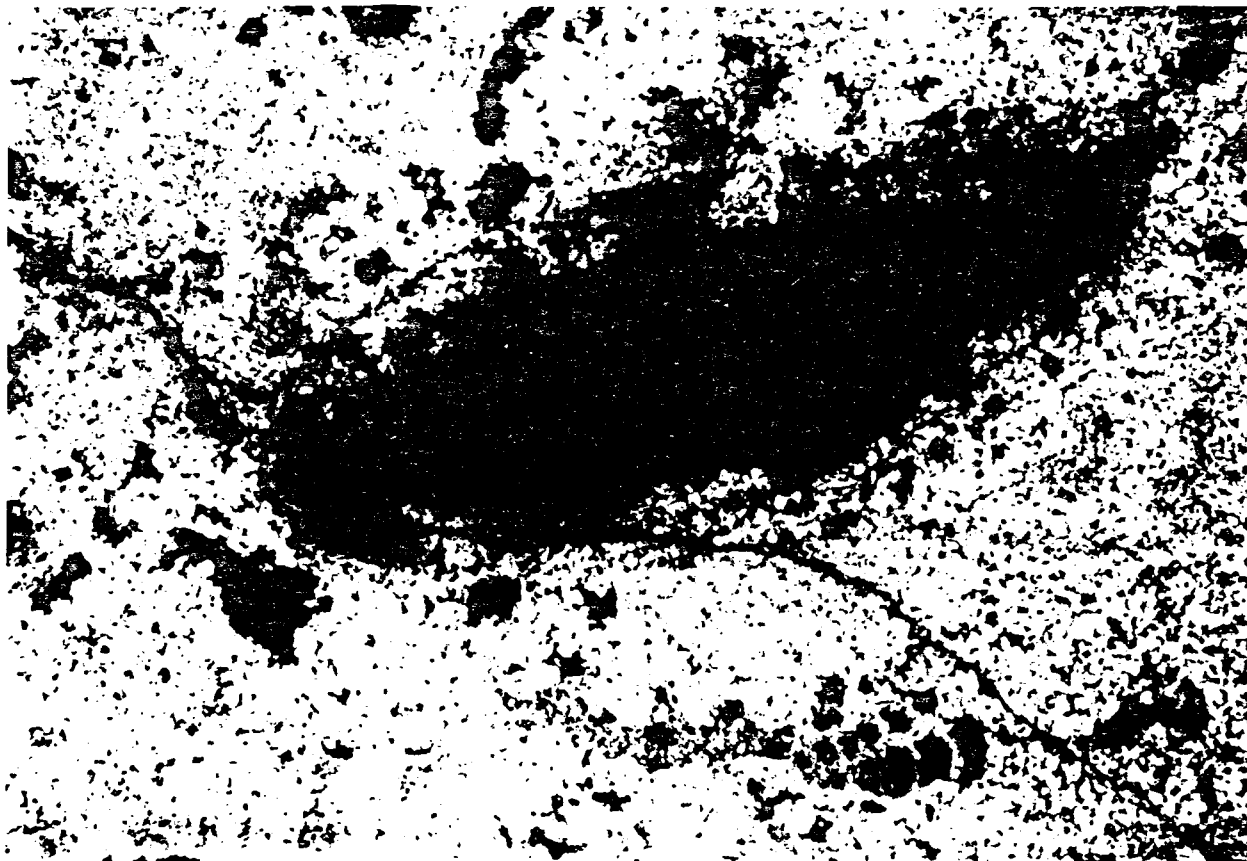


Fig. 4.53 Thin section of Maljamar San Andres core M-1 (25x) showing vugs and fractures. Porosity is black.

simple analysis presented here is only a first step, but a necessary one, toward understanding mixing in the complex flows which occur in actual CO₂ floods in reservoir rocks.

4.6 Summary and Conclusions

In this chapter results of twenty-one miscible displacements in sandstones and seventeen similar displacements in carbonate core samples are presented. The displacements were performed in an apparatus that allows on-line effluent composition analysis in both single-phase and two-phase displacements. Displacement results were interpreted using the Coats-Smith model. An analysis of numerical dispersion showed that a simple finite difference representation could be used to solve the flow equations efficiently. Results of single-phase miscible displacements in most of the carbonates differed sharply from those in the sandstones, though there was one carbonate sample for which displacement results were much like those in the sandstones. An analysis of thin sections of the core materials was undertaken to examine the relationship between mixing and pore structure. The experimental evidence and analysis given leads to the following conclusions:

- (1) Dispersion coefficients for sandstones determined by on-line refractive index analyses of effluent compositions agreed well with values reported by other investigators. Dispersion coefficients for all the samples varied approximately linearly with average interstitial velocity.
- (2) Flowing fractions for the Berea and Frannie sandstone samples were very close to one. The Rock Creek sandstone showed flowing fractions slightly less than one at high average interstitial velocities. Observation of thin sections of the core materials indicated that all of the sandstones were much more uniform than most of the carbonates but that the Rock Creek sample was the most heterogeneous of the sandstones.
- (3) A qualitative analysis of the effect of pore structure on mixing in single-phase flow suggests that a wide distribution of pore sizes is necessary but not sufficient to produce a flowing fraction less than one. Also required are connections between pores which create preferential flow paths. Thus, mixing effects which, on average for the scale of the displacement, lead to early breakthrough and a low flowing fraction result from nonrandom microscopic heterogeneity in the pore structure.
- (4) Carbonate core samples (Seminole, San Andres Outcrop and Maljamar) which showed broad pore size distributions and preferential flow paths in thin sections also showed flowing fractions significantly less than one. The Wasson carbonate core did not show such heterogeneity and also showed no evidence of mixing between stagnant and flowing streams.

- (5) Flowing fractions decreased slightly with increasing velocity for two carbonate samples with the broadest pore size distributions. For the other samples, flowing fractions were independent of velocity.
- (6) Dispersion and mass transfer coefficients for the carbonates also depended approximately linearly on average interstitial velocity. Dispersion coefficients were significantly higher for carbonates than for sandstones.
- (7) Average mixing behavior on the scale of short laboratory cores is qualitatively consistent with observations of pore structure on the scale of thin sections.
- (8) Significant trapped fractions were observed in both wetting and nonwetting phases in a Seminole carbonate core. Additional experiments are needed to check the validity of this result.

5. ONE-DIMENSIONAL SIMULATION: INTERACTIONS OF PHASE BEHAVIOR WITH MIXING IN UNIFORM AND HETEROGENEOUS POROUS MEDIA

The complexity and variety of the physical effects which combine to determine the performance of a field scale CO₂ flood makes detailed simulation of a field displacement process a formidable task. No simulator currently available models all of the factors known to influence CO₂ flood performance (Orr, Silva, Lien & Pelletier 1982; Orr & Taber 1982). Nevertheless, simulation of even a limited collection of the process mechanisms is an important part of building understanding of the interactions of mechanisms inherent in the complex flows which develop during a CO₂ flood. Sensitivity of process performance to variations in phase behavior, fluid properties and other process variables can be investigated far more rapidly by simulation than by experiments. Such studies are convincing, however, only if the simulator can be shown to be quantitatively reasonable for the flows it attempts to model. In §5.1, we report results of a test of the accuracy of the one-dimensional simulator in which the performance of slim tube displacements is predicted. While those displacements are substantially simpler than the flows which occur in reservoir rocks, they are a useful test of the predictive power of the simulator because the flow is very nearly one-dimensional and is strongly influenced by phase behavior. Clearly, it is important to establish whether the simulator is accurate for simple flows before more complex tests are attempted.

In addition, modifications to the one-dimensional simulator to include the effects of dendritic and trapped saturations in the oil phase are described. The formulation of the new model and results of tests performed to validate the numerical scheme are discussed in §5.2. Results of extensive simulation runs to examine the consequences of heterogeneity of the pore structure or alterations to mixing due to high water saturations are summarized in §5.3.

5.1 Quantitative Prediction of Slim Tube Displacement Performance

Simulations of slim tube displacements of Maljamar crude oil by CO₂ at four pressures were performed using a simple one-dimensional simulator similar to those described by Pope and Nelson (1978), Gardner, Orr, and Patel (1981) and Orr (1980) but with one important difference. It models the effects of volume change on mixing by allowing each component to have a different density in each phase. In it, the oil is represented as two components, with CO₂ as the third component. Material balance equations for the three components are solved by an explicit finite difference method which allows the use of numerical dispersion to model qualitatively the effects of physical dispersion.

The calculations performed in the simulator are based on the following assumptions:

- (1) Darcy's law describes the flow of each of up to three phases.
- (2) The flow system has uniform cross section and properties, and fluids are uniform and well mixed in the direction transverse to flow.
- (3) Capillary pressure effects are negligible.
- (4) Local chemical equilibrium exists between phases.
- (5) The density of a phase can be calculated as a volume weighted average of constant apparent densities of each component in that phase.
- (6) Changes in pressure over the length of the displacement have negligible effect on the compositions and densities of the CO₂-hydrocarbon mixtures.
- (7) CO₂-crude oil phase behavior can be represented in terms of three components: CO₂, light hydrocarbons, and heavy hydrocarbons.

Material balance equations for each component in the system have the form

$$\frac{\partial}{\partial \tau} \sum_j \rho_j x_{ij} S_j + \frac{1}{q_i} \frac{\partial}{\partial \xi} \sum_j \rho_j x_{ij} F_j q = 0 \quad i = 1, n_c \quad (5.1)$$

where $\tau = (q_i t)/(\phi AL)$ is the dimensionless time scale based on the volumetric injection rate q_i , t the time, ϕ , A and L the porosity, cross-sectional area and length of the slim tube, ρ_j , F_j and S_j the molar density, fractional flow and saturation of phase j , x_{ij} the mole fraction of component i in phase j , $\xi = x/L$ the dimensionless length, and q the local volumetric flow rate. The molar density of phase j is defined as

$$\rho_j = \left[\sum_i \left(x_{ij} / \rho_{ij} \right) \right]^{-1} \quad (5.2)$$

where ρ_{ij} is the apparent molar density of component i in phase j . The fractional flow of phase j is defined as

$$F_j = \frac{k_{rj}/\mu_j}{\sum_i k_{ri}/\mu_i} \left\{ 1 - \frac{A k g \sin \alpha}{q} \left[\sum_i \frac{k_{ri}}{\mu_i} (M_i \rho_i - M_j \rho_j) \right] \right\} \quad (5.3)$$

where α is the dip angle, g gravity, and M_i and M_j are average molecular weights of phases i and j .

In finite difference form, eq. (5.1) is

$$\left(\sum_j \rho_j x_{ij} S_j \right)_m^{n+1} = \left(\sum_j \rho_j x_{ij} S_j \right)_m^n - \frac{\Delta \tau}{q_i \Delta \xi} \left\{ \left(\rho_j x_{ij} f_{jq} \right)_m^n - \left(\rho_j x_{ij} f_{jq} \right)_{m-1}^n \right\} \quad (5.4)$$

where m is the grid block and n the time step. Eq. (5.4) is used to calculate new overall compositions in each grid block. Phase behavior and fluid property routines then calculate new phase compositions, densities, and viscosities. Finally, fractional flows and local flow rates are calculated and the process repeated. Adjustments that result from volume change on mixing are made through the local flow rate. After fluids that have flowed a grid block are mixed with the fluids present in the block, the volume of the mixture will differ from the grid block volume as components transfer between phases in which they have different densities. If after mixing, the volume of the new mixture is less than the grid block volume, then a portion of the flow into the block during the next time step is used to make up the volume change and the flow out of the block is reduced correspondingly. If the volume increases during mixing, then the flow rate out of the block is greater than the flow rate into it.

The finite difference form applied here allows the use of time truncation error to cancel a portion of the spatial truncation error which provides some control of the level of numerical dispersion (Lantz 1971). Numerical dispersion can be used to model physical dispersion quantitatively as long as only one phase is flowing. When two phases are flowing, however, less control is possible because the nonlinearity of the fractional flow functions alters the level of numerical dispersion in such a way that it is no longer constant throughout the grid (Lantz 1971; Orr 1980). For instance, the composition and saturation profiles in Fig. 5.6 show evidence of more numerical dispersion in the single phase regions than in the two-phase portions of the flow. The simulations reported here were all performed with 100 grid blocks and a time step size of 0.00125, which represents a compromise between numerical dispersion, stability and computation cost. It should be noted that the dispersion, numerical or physical, does alter computed composition paths and hence oil recovery (Gardner, Orr & Patel 1981).

Simple polynomial representations of ternary diagrams are used to enter the phase behavior data into the simulator (Orr 1980). Phase behavior of mixtures of CO_2 with Maljamar crude oil was measured using the continuous multiple contact experiment (see Orr, Silva & Lien 1983 for details of the experiments). Pseudo-ternary phase diagrams obtained in those experiments, all of which were performed at 32°C (90°F), are shown in Figs. 5.1-5.4 for four pressures, 5520, 6890, 8270 and 9650 kPa (800, 1000, 1200 and 1400 psia).

Detailed gas, liquid, and phase composition data are available separately (Silva et al 1982b; Silva et al 1981a, b & c). In the displacement at 5520 kPa, only a small portion of the phase diagram was scanned because very small amounts of hydrocarbons were extracted into the upper (vapor) phase (Fig. 5.1). The vapor phase was nearly pure CO_2 and hence, the composition of the oil in the cell changed little during the displacement. A CO_2 flood of Maljamar separator oil at 5520 kPa would be immiscible.

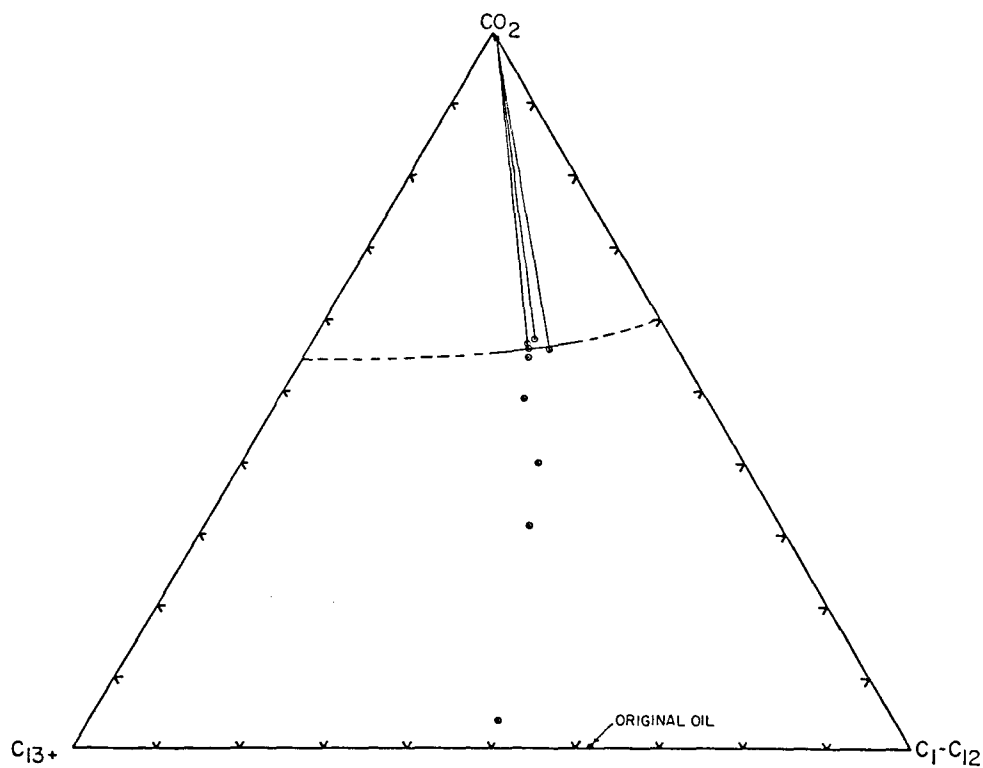


Fig. 5.1 Pseudo-ternary representation of phase compositions for mixtures of CO₂ with Maljamar separator oil at 5520 kPa and 32°C.

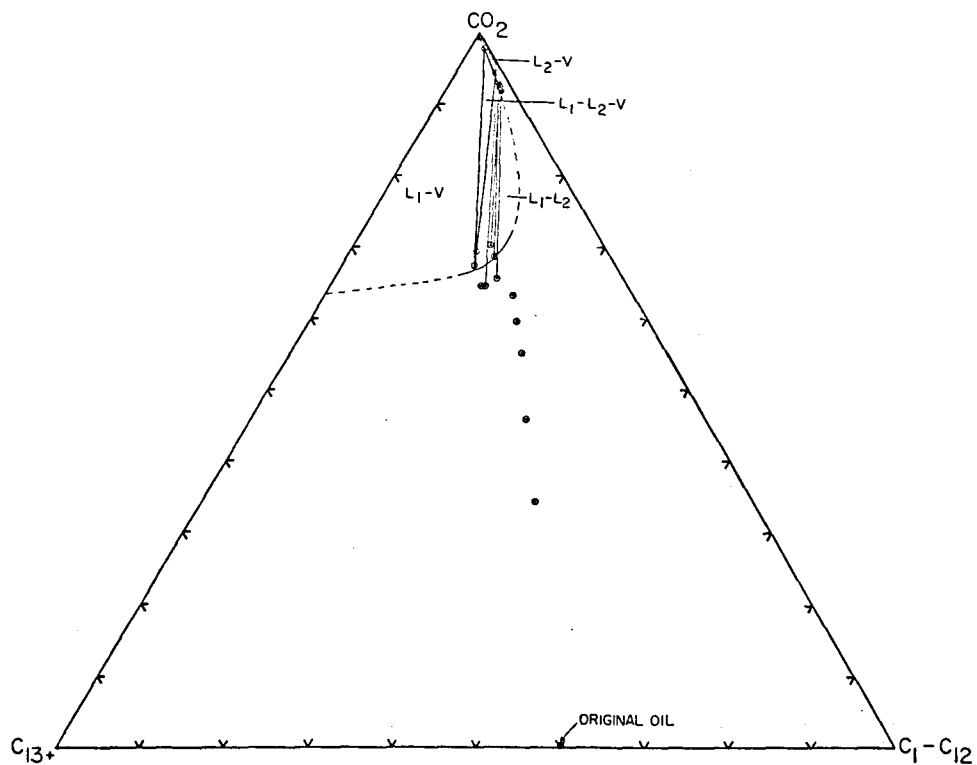


Fig. 5.2 Pseudo-ternary representation of phase compositions for mixtures of CO₂ with Maljamar separator oil at 6890 kPa and 32°C.